ISSN: 1813-1786
Indexed In:
ULRICH'S P. D.
PASTIC

TECHNICAL JOURNAL
SPECIAL ISSUE
ON
VIBRATION ANALYSIS

2012

University of Engineering and Technology
Taxila

HEC Recognized

Dr. Muhammad Abbas Choudhary
Patron In-chief

Dr. Abdul Razzaq Ghumman
Chief Editor

Mrs Nuzhat Yasmin
Editor

ISSN: 1813-1786

Yearly Published
Volume No. 17
2012

Technical journal is abstracted and indexed in Agris, Pakistan Science abstract, Ulrich periodic directory plus Pastic indexing service.

Technical Journal is annual peer reviewed publication of UET Taxila published regularly with the key objective to provide the academic and researchers to disseminate new knowledge and technology for the benefit of everyone ranging from academic and professional research communities to industry practitioners in a wide range of topics in: Electrical Engineering, Mechanical Engineering, Mechatronics Engineering, Civil Engineering, Computer Engineering, Software Engineering, Telecommunication Engineering, Environmental Engineering, Industrial Engineering And Applied Sciences. Views expressed in the journal are only those of authors and do not necessarily reflect those of U.E.T. Taxila or the author.

It is a pleasure to present the 17th annual volume of Technical Journal containing research papers in 'Engineering and Technology' published by the University of Engineering and Technology, Taxila.. The journal gives researchers the opportunity to present full accounts of their work, its rationale, findings and conclusions. Additionally, it is worth mentioning that the university also published a special issue on “Vibration Analysis”.

This is a special volume on Vibration Analysis. Vibration analysis is used to detail the early precursors to machine failure, allowing machinery to be repaired or replaced before an expensive failure occurs. It is conducted through hand held or permanently positioned accelerometers placed on Key measurement points on the equipment commonly used on most large items of rotating equipment such as tubines, Centrifugal pumps motors, gear boxes etc.

The volume includes six papers by eminent scholars of Pakistan. I hope the research presented in these papers will be beneficial for the research institution and the students studying in mechanical engineering.

Nuzhat Yasmin
Editor

EDITORIAL BOARD

● CONTENTS

Discover papers in this journal online http://techjournal.uettaxila.edu.pk

Seismic Analysis of Electronic Cabinet using ANSYS

M. Waqas Anjum[1], Basit Khalid[2] and Abdul Rehman[3]

Abstract

Structural analysis using Finite Element Method gives a preliminary assessment of dynamic behavior of mechanical structures in order to establish the guidelines for designing the experiment. The main objective of this study was to develop a methodology of seismic analysis of electronic cabinets using ANSYS. Generally, two approaches i.e. transient analysis and response spectrum analysis are adopted for the seismic analysis in ANSYS. Since, the given loading was in time domain, therefore, transient structural analysis was preferred for the detailed dynamic investigation of electronic cabinet. The cabinet was modeled with Beam188 and its modal analysis was performed rendering the fundamental natural frequency of 8.94Hz, sufficiently close to the experimentally measured frequency of 8.33Hz. Subsequently, Transient analyses were performed for horizontal components of ground motion that resulted in peak displacement of 37mm and 28mm at the top of the cabinet which were in good agreement with experimentally measured maximum displacement of 40mm and 30mm at the same location, respectively. In addition, peak accelerations obtained from transient analyses were 0.6g and 0.82g while the experimentally measured peak accelerations were 0.8g and 0.89g respectively. It can be concluded that transient analyses in ANSYS produced equivalently reliable assessment of dynamic behavior of electronic cabinets.

Key words: Transient analysis, Modal analysis, Structural analysis, Seismic analysis.

Introduction

Locally, one of the departments of Pakistan Atomic Energy Commission (PAEC) was to install various electronic cabinets at some nuclear facility situated in seismically active zone. It is a common practice to conform the functionality and integrity of structures experiencing strong ground motions before their field installation. Therefore, seismic analysis of these electronic cabinets becomes necessary. Seismic analysis is a subset of structural analysis that is used for the calculation of the response of a structure to earthquakes. It gives complete picture of the behavior of structure subjected to seismic event. It is part of the process of structural design, earthquake engineering or structural assessment and retrofit in regions where earthquakes are frequently prevalent. Earthquake Engineering Centre (EEC) of Department of Civil Engineering, UET Peshawar was contacted for experimental testing and seismic qualification. A series of shake table tests of these cabinets were performed at EEC for various time histories and the performance of these cabinets were found satisfactory under the given conditions Ali M. (2011).

It is a common practice that numerical simulations are performed before experimental testing of prototype structures in order to establish the guidelines of designing the experiment. This also serves to save time and cost involved in experimentation. In this work, the availability of experimental data enables us to validate the simulated results when compared with experimental measurements in order to establish an equivalently reliable approach for experimental testing in future.

Seismic Analysis in ANSYS Finite Element Model

The finite element model of electronic cabinet was developed using beam element (BEAM188) as shown in Figure 1. BEAM188 has six or seven degrees of freedom at each node. These include translations in the x, y, and z directions and rotations about the x, y, and z directions. A seventh degree of freedom (warping magnitude) is optional. This element is well-suited for linear, large rotation, and/or large strain nonlinear applications. The beam element is a one-dimensional line element in space. The cross-section details are provided separately by a section that is associated with the beam element having unique reference identity Ansys (2007). All members in numerical model are assigned ASTM A36 steel having the following properties. Modulus of Elasticity, E= 200GPa Poisson Ratio, v= 0.3 Density, ρ= 7850 kg/m3

[1,2 & 3]Instrumentation Control and Computer Complex (ICCC), PAEC, Islamabad

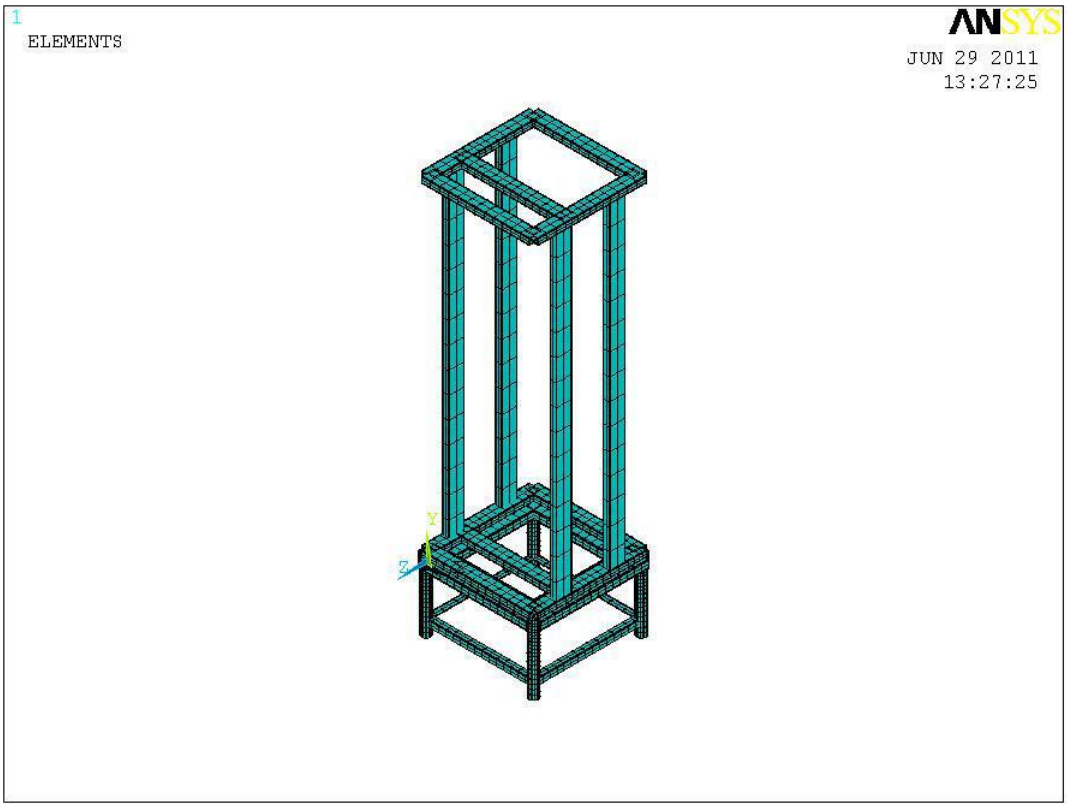

Figure 1: FE model of cabinet

The model was constrained in all degrees of freedom at its base. These boundary conditions were used to simulate the experimental situation where base frame was fixed in the concrete pad.

Modal Analysis

Modal analysis, also known as free vibration analysis, is used to determine the natural frequencies and mode shapes of a structure. Modal analysis of electronic cabinet was performed to determine the vibration characteristics, natural frequencies and mode shapes, of cabinet. Block 3 Lanczos method was used to extract the eigenvalue (natural frequency) and eigenvectors (mode shape) of the cabinet. First 10 modes of vibration of electronic cabinet were extracted and their corresponding natural frequencies are given in Table 1 below. Table 1 Natural frequency.

Table 1: Natural frequencies V/S Mode No.

Mode No.	Natural frequency (Hz)
1	8.94
2	17.09
3	24.19
4	51.44
5	57.57
6	58.46
7	59.63
8	82.86
9	88.27
10	93.75

Transient Analysis

Generally, two approaches are adopted in ANSYS for seismic analysis. They are the transient analysis and response spectrum analysis. Former approach gives detailed response of the dynamic behavior of the structure while the latter approach only gives the peak response of structure Ansys (2007). As, the seismic loading was also in time domain, therefore, transient analysis was preferred for detailed investigation of dynamic response of cabinets.

Displacement time histories recorded at concrete pad during shake table test were used as input seismic load for the transient analysis. Two displacement time histories; 1H (horizontal in direction-1 i.e. parallel to the door of cabinet) and 2H (horizontal in direction-2 i.e. orthogonal to direction-1) were used as input load at the base with a constant modal damping of 5% as specified by EEC Ali M. (2011). Both displacement time histories are given in Figure 2 and Figure 3 respectively.

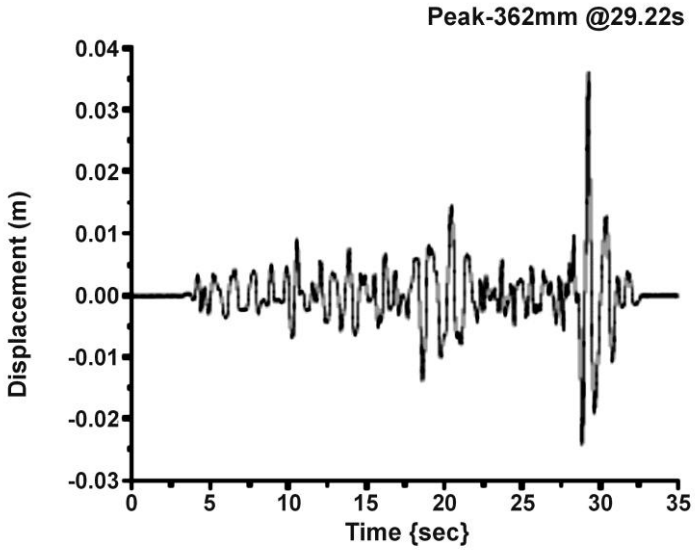

Figure 2: 1H displacement load

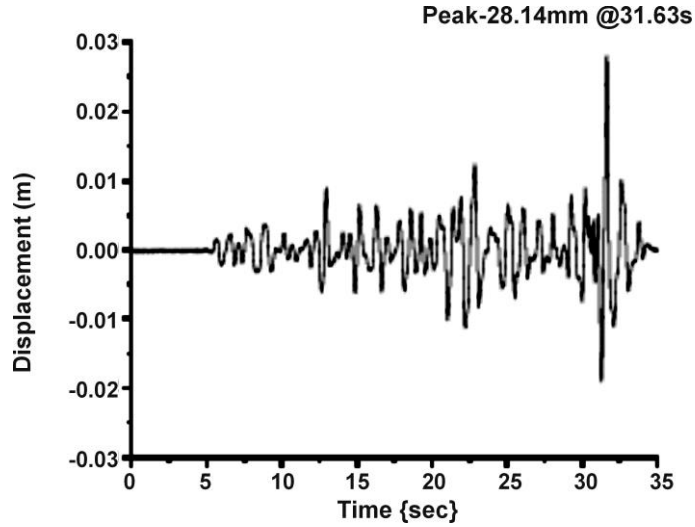

Figure 3: 2H displacement load

Results and Discussion

The fundamental frequency of the cabinet obtained from modal analysis was 8.94Hz, see Table.1, sufficiently close to the experimentally obtained frequency of 8.33Hz Ali M. (2011).

1H Loading

The maximum displacement of the cabinet was found to be 37.02mm @29.22sec at the top corresponding to the location exactly where the displacement transducer was actually installed and is shown in Figure 4. The peak acceleration was 0.59g at accelerometer location and is shown in Figure 5.

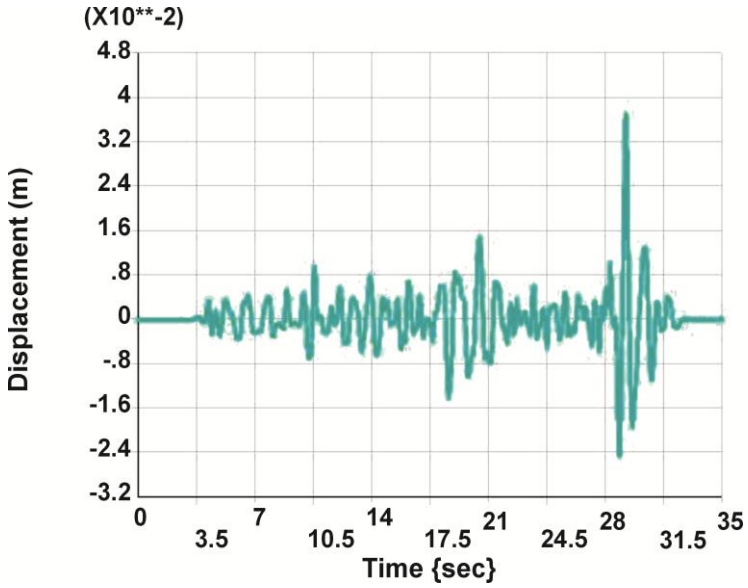

Figure 4: Displacement response corresponding to 1H

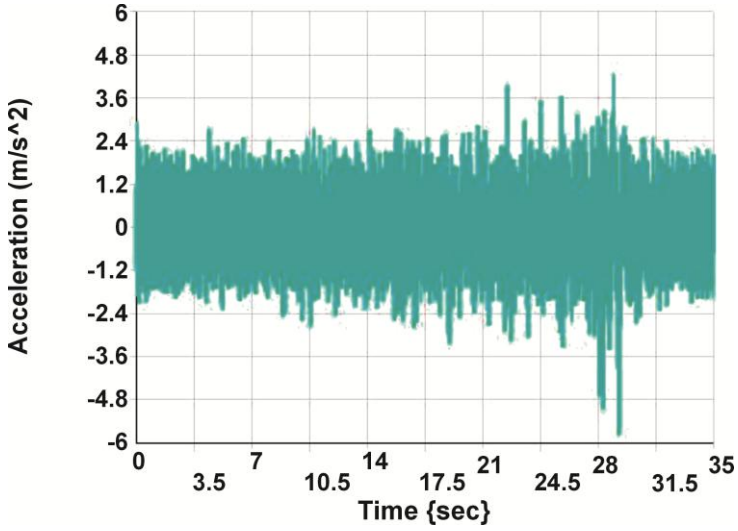

Figure 5: Acceleration response corresponding to 1H

Figure 4 shows the maximum displacement of 37.02mm@29.22sec obtained from transient analysis at

the top of the cabinet (i.e. location of displacement transducer). The maximum displacement obtained experimentally was 40mm@29.22 sec, shown in Figure 6. Both the numerical and experimental displacement values were in good agreement with each other. However, peak acceleration obtained from transient analysis was 0.6g shown in Figure 5 while the experimentally measured peak acceleration was 0.8g and is shown in Figure 7.

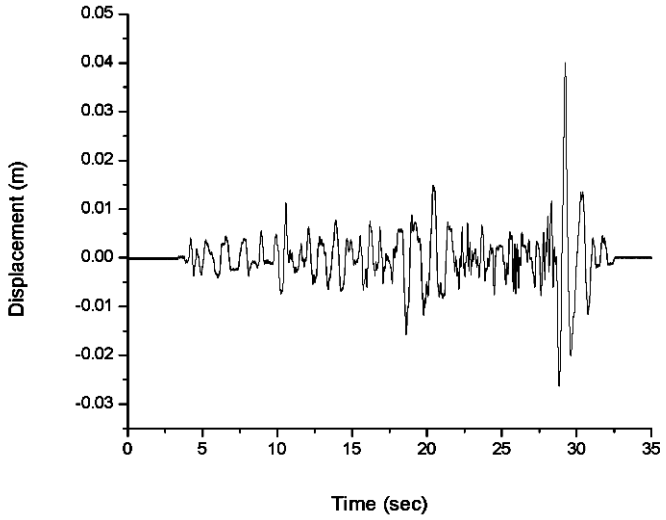

Figure 6: Displacement response (experimental)

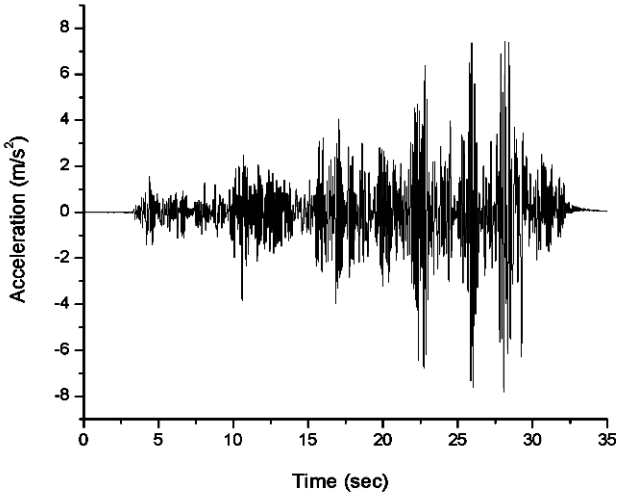

Figure 7: Acceleration response (experimental)

For 2H loading the maximum displacement of the cabinet was found to be 28.33mm @31.63sec at the top corresponding to the location exactly where the displacement transducer was actually installed and is shown in Figure 8. The peak acceleration was 0.82g at accelerometer location and is shown in Figure 9.

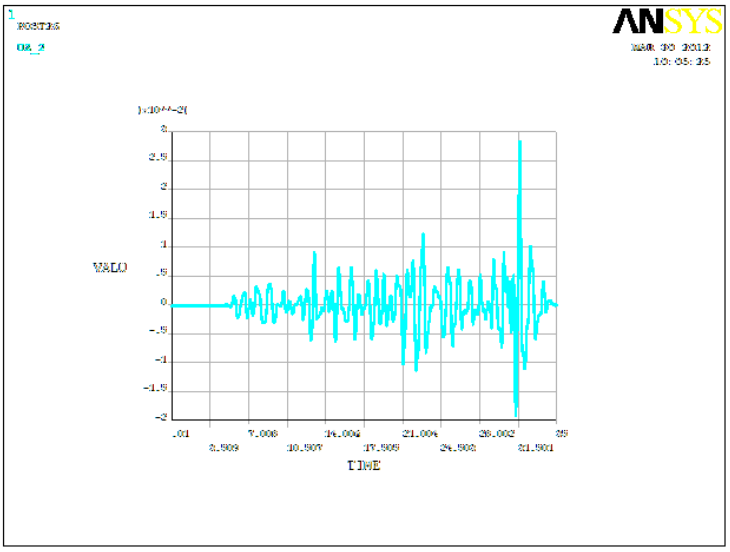

Figure 8: Displacement response corresponding to 2H

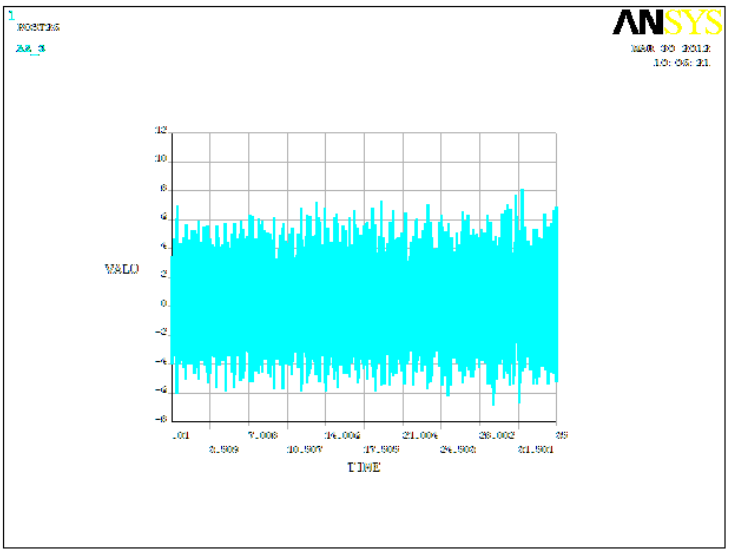

Figure 9: Acceleration response corresponding to 2H

Figure 8 shows the maximum displacement of 28.33mm @31.63sec obtained from transient analysis at the top of the cabinet (i.e. location of displacement transducer). The maximum displacement obtained experimentally was 30.44mm@31.63 sec, shown in Figure 10. Both the numerical and experimental displacement values were in good agreement with each other. However, peak acceleration obtained from transient analysis was 0.82g shown in Figure 9 while the experimentally measured peak acceleration was 0.89g and is shown in Figure 11.

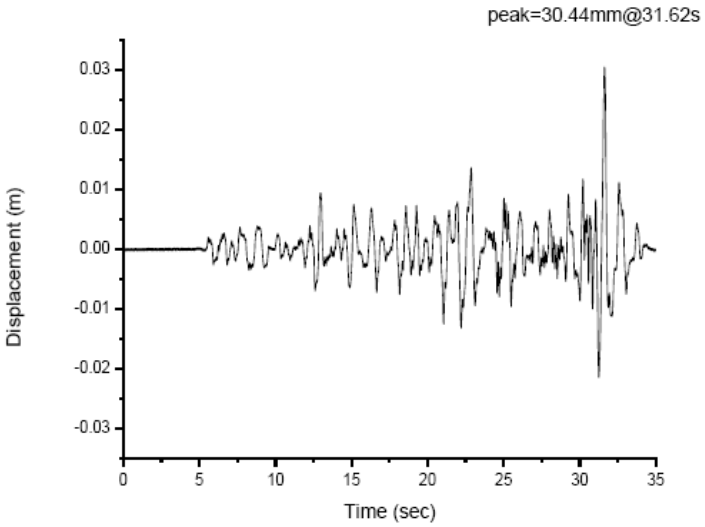

Figure 10: Displacement response (experimental)

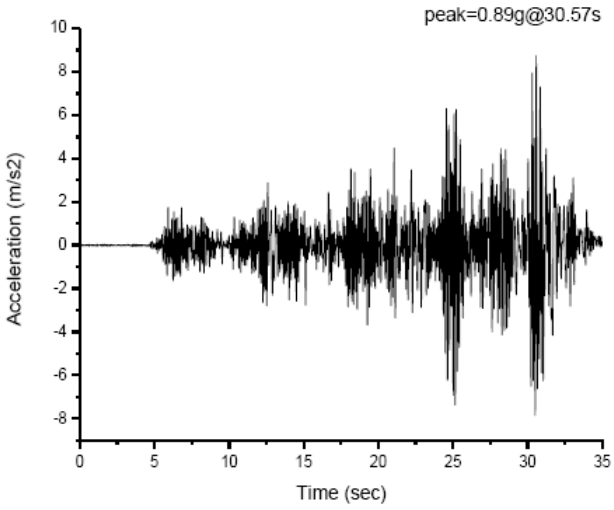

Figure 11: Acceleration response (experimental)

Conclusion

It can be concluded that seismic analysis performed in ANSYS produced equivalently reliable assessment of the dynamic behavior of electronic cabinets. Although, ANSYS simulations cannot exclude the experimentations but greatly reduce the design of experiments where time and cost do not allow experimentations.

Reference

[1] Ali M., (2011), “Seismic Qualification of Electronic Cabinets for Pakistan Atomic Energy Commission”, Earthquake Engineering Centre, UET Peshawar, Final Report.

[2] ANSYS, ANSYS (2007), Structural Analysis Guide, ANSYS, Inc.

Effects of Impulsive Loading on Reinforced Concrete Structures

Saeed Ahmad[1], Mehwish Taseer[2], Huma Pervaiz[3]

ABSTRACT

This paper presents the summary of the work done in civil engineering department, UET Taxila to evaluate reinforced structural elements under impulsive loading. Part of this work has been published elsewhere separately. The experimental work was carried out in the suburbs of Hassan Abdal hills by constructing different wall panels. In this paper a set of four reinforced concrete walls with varying thickness were constructed. These walls were tested with varying explosive loads and scaled distance. Pressure sensors, accelerometers, dynamic strain amplifier, data acquisition board and strain gauges were used to measure air blast and ground shock parameters. Acceleration and the pressure time history at different points are recorded. Empirical relationships have been developed for various blasts loading parameters are compared with the results of previous researchers. In the light of TM 5-855 comparison is made on the basis of air blast and ground shock parameters with the results obtained from Conwep. Detailed analysis of walls subjected to blast loads is carried out using Sap 2000 (Ver. 14). Reinforced concrete wall was designed for blast loading using methodology described in UFC_3_340_02. It is concluded that consideration of air blast and ground shock pressure are important for accurate analysis of structure response of structures.

Keywords: Scaled distance, ground shock, the pressure time history, impulsive loading

Introduction

In the past few decades considerable emphasis has been given to problems of impulsive loading e.g., blast loads and earthquakes. Due to different accidental or intentional events, the behavior of structural components subjected to impulsive loads specifically blast loading has been the subject of considerable research effort in recent years.

Conventional structures, particularly that above grade, normally are not designed to resist impulsive loads; and because the magnitudes of design loads are significantly lower than those produced by most explosions, conventional structures are susceptible to damage from explosions. With this in mind, developers, architects and engineers increasingly are seeking solutions for potential blast situations, to protect building occupants and the structures.

In the design of protective structures to resist the effects of accidental explosions, the principal effects of the explosive output to be considered are blast overpressures referred to as blast pressures. Fragments generated by the explosion and the shock loads produced by the shock wave transmitted through the air or ground. Of these three parameters, the blast pressures are usually the governing factors in determination of the structure response. However, in some situations, fragments and/or shock loads may be just as important as the pressures in determining the configuration of the facility.

The impulsive effects of an explosion are in the form of a shock wave composed of a high intensity shock front which expands outward from the surface of the explosive into the surrounding air. As the wave expands, it decays in strength, lengthens in duration, and decreases in velocity. This phenomenon is caused by spherical divergence as well as by the fact that the chemical reaction is completed, except for some afterburning associated with the hot explosion products mixing with the surrounding atmosphere.

As the wave expands in air, the front impinges on structures located within its path and then the entire structure is engulfed by the shock pressures. The magnitude and distribution of the blast loads on the structure arising from these pressures are a function of the following factors: (1) explosive properties, namely type of explosive material, energy output (high or low order detonation), and weight of explosive; (2) the location of the detonation relative to the protective structures; and (3) the magnitude and reinforcement of the pressure by its interaction with the ground barrier, or the structure itself.

1-3 Department of Civil Engineering, University of Engineering and Technology Taxila

Experimental Setup

Experimental data is shown in tabular form below:

Table 1: Experimental Data

Wall	Geometry			Stand-off Distance (m)	Charge Weight (kg)	TNT Equivalent (kg)	Scaled Distance (m/kg$^{1/3}$)
	Thickness (in)	Width (m)	Clear Height (m)				
Wall 1	5	2	2	2.87	1	0.6	3.4
				2.87	2	1.2	2.7
				2.87	4	2.4	2.1
Wall 2	6.7	2	2	2.87	1	0.6	3.4
				2.87	2	1.2	2.7
				2.87	4	2.4	2.1
Wall 3	6.4	2	2	2.87	1	0.6	3.4
				2.87	2	1.2	2.7
				2.87	4	2.4	2.1
Wall 4	6.4	2	2	2.87	1	0.6	3.4
				2.87	2	1.2	2.7
				2.87	4	2.4	2.1

Location of the Sensor and Accelerometer for measuring pressure and acceleration respectively are shown in below sketch.

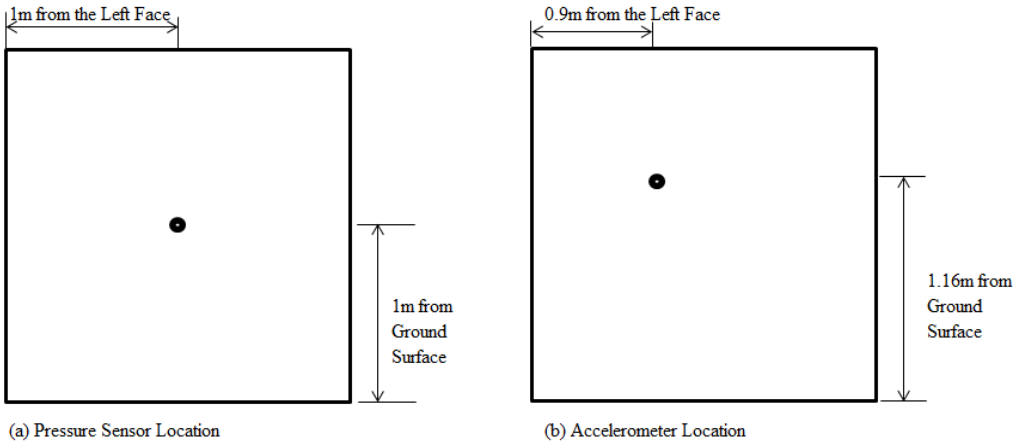

Figure 1: Location of Gauge

Analytical Approaches

SAP2000 is used for detailed analytical analysis of RCC walls under impulsive loading. Input to SAP was extracted from the experimental data. Stresses and moments are noted and shown in below tables.

Table 2: Stress Summary at Wall

Explosive Load	S11 (psi)	S22 (psi)	S12 (psi)
1kg	75.78	140.07	50.377
2kg	152.42	281.73	101.32
4kg	487.26	923.87	337.38

Table 3: Moment Summary at Wall

Explosive Load	M11 (kip-ft/ft)	M22 (kip-ft/ft)	M12 (kip-ft/ft)
1kg	2.77	5.186	1.744
2kg	5.572	10.43	3.51
4kg	7.94	14.85	11.68

ConWep is used for calculating the peak free-field stress due to the directly transmitted shock wave, and optionally allows the addition of a reflected wave from a deeper layer and a relief (tension) wave reflected from the ground surface. Peak particle velocity, acceleration, and displacement are calculated using the direct path only-- reflections from the surface or a lower layer are not included. The output summary of analysis performed using ConWep is shown in below table.

Table 4: Output Summary of ConWep Analysis

TNT Equivalent Weight (kg)	Range (m)	Scaled Distance ($m/kg^{1/3}$)	P_{so} (kPa)	PPA (m/s2)
0.6	2.87	3.40	77.87	134.2
1.2	2.87	2.70	135.6	233.6
2.4	2.87	2.14	236.1	406.7

Results and Discussions

Peak Pressure

Experiments have yielded the following equation for P_{so} with respect to the scaled distance.

$$P_{so} = 1595.6 \left(\frac{R}{Q^{1/3}}\right)^{-2.868}$$

Where P_{so} is in kPa, R is in meters and Q is TNT equivalent charge weight in kg. This relationship is valid for small stand-off distances i.e., R ≤ 5m. This equation has been compared with other empirical formulae as mentioned in below table.

Table 5: Comparison of Empirical Equations for P_{so}

TNT Weight (kg)	Range (m)	Scaled Distance ($m/kg^{1/3}$)	P_{so}					
			Brode Eq. (kPa)	Henrych Eq. (kPa)	Chengqing Eq. (kPa)	Javed Iqbal Eq. (kPa)	Adeel Eq. (kPa)	Current Research (kPa)
0.6	2.87	3.4	53.8	62.9	86.2	97.9	97.9	47.7
1.2	2.87	2.7	83.8	97.2	136.5	153.1	197.2	92.4
2.4	2.87	2.14	135.1	151.68	217.8	237.8	326.8	180

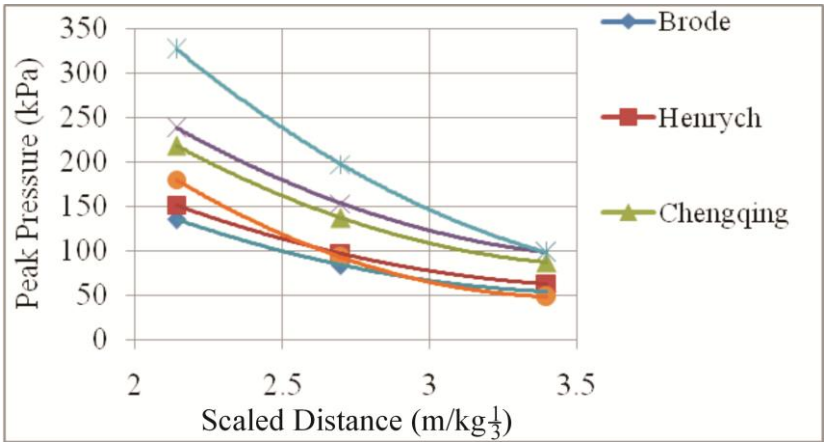

Figure 2: Graph Showing Comparison of Empirical Equations for P_{so}

It shows that the equation derived through experiments is in close relation with Brode's and Henrych's empirical results. Similarly the experimental results are compared with the results obtained from ConWep analysis.

Table 6: Comparison of ConWep and Experimental Output for Pso

Explosive Weight (kg)	Range (m)	Scaled Distance ($m/kg^{1/3}$)	P_{so} (kPa)	
			ConWep	Experimental
0.6	2.87	3.40	77.9	71.7
1.2	2.87	2.70	135.5	137.8
2.4	2.87	2.14	236	234.4

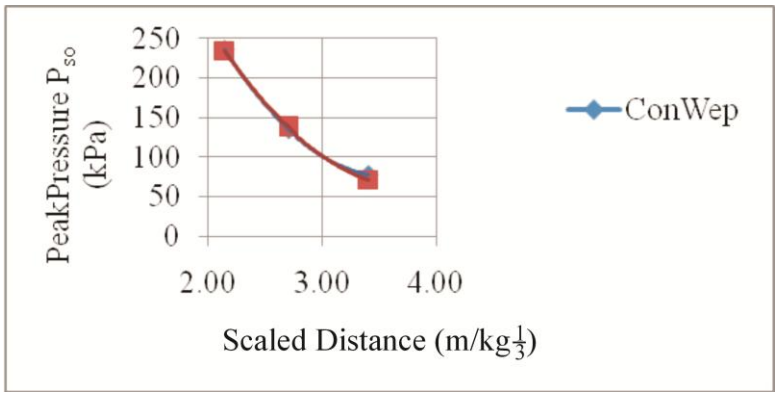

Figure 3: Comparison of ConWep Results with Experimental Output for Pso

Shock Wave Front Arrival Time

The best fitted curve yields the following equation.

$$T_a = \frac{4.637}{C_a}\left(\frac{R}{Q^{1/3}}\right)^{-0.138}$$

Where T_a is in sec, R is the range in meters and Q is the TNT charge weight in kg. C_a is the velocity of sound in air taken as 340m/s. Previous research by Adeel gives following equation.

$$T_a = \frac{6.46}{C_a}\left(\frac{R}{Q^{1/3}}\right)^{-0.41}$$

Table 6: Comparison of Empirical Equations for Ta

TNT Weight (kg)	Range (m)	Scaled Distance ($m/kg^{1/3}$)	Ta	
			Adeel Eq. (msec)	Current Research (msec)
0.6	2.87	3.4	11.5	11.52
1.2	2.87	2.7	12.6	11.89
2.4	2.87	2.14	13.9	12.27

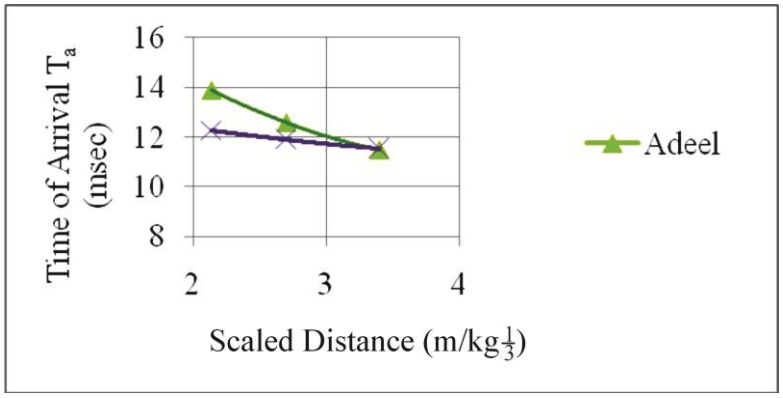

Figure 4: Graph Showing Comparison of Empirical Equations for Ta

Positive Phase Duration of the Shock Wave

The duration of the positive phase of the shock wave is the summation of the rising time to the maximum pressure and the decreasing time to the ambient pressure.
So

$$T_a = T_r + T_d$$

The experiments yield following relationships

$$T_r = 0.3108 \left(\frac{R}{Q^{1/3}}\right)^{-0.1}$$

$$T_d = 2.462 \left(\frac{R}{Q^{1/3}}\right)^{-0.472}$$

Therefore T can be written as

$$T = 0.3108 \left(\frac{R}{Q^{1/3}}\right)^{-0.1} + 2.462 \left(\frac{R}{Q^{1/3}}\right)^{-0.472}$$

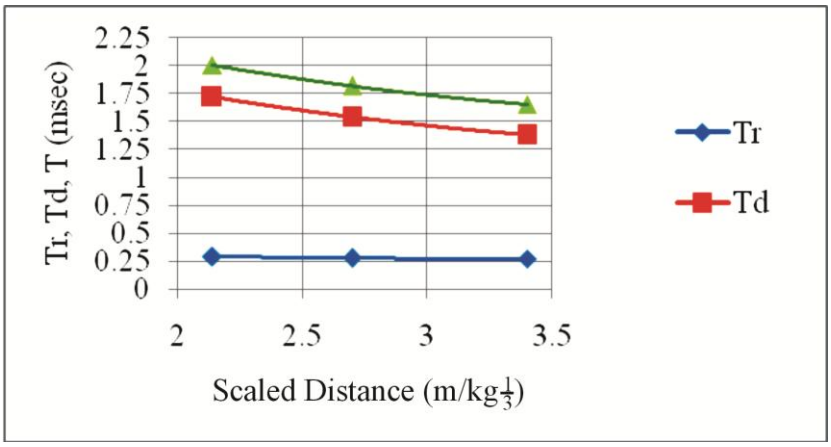

Figure 5: Graph Showing Positive Phase Duration of the Shock Wave

Peak Particle Acceleration

The experiments yield following equation for the PPA against scaled distance

$$PPA = 250.43 \left(\frac{R}{Q^{1/3}}\right)^{-2.361}$$

Where PPA is in terms of acceleration of gravity in m/s^2, R is in meters and Q is TNT equivalent charge weight in kg. The experimental results are compared with that obtained from ConWep.

Table 7: Comparison of ConWep and Experimental Output for PPA

Explosive Weight (kg)	Range (m)	Scaled Distance ($m/kg^{1/3}$)	PPA, g's (m/s^2)	
			ConWep	Experimental
0.6	2.87	3.40	13.68	13.5
1.2	2.87	2.70	23.81	25.4
2.4	2.87	2.14	41.45	40.2

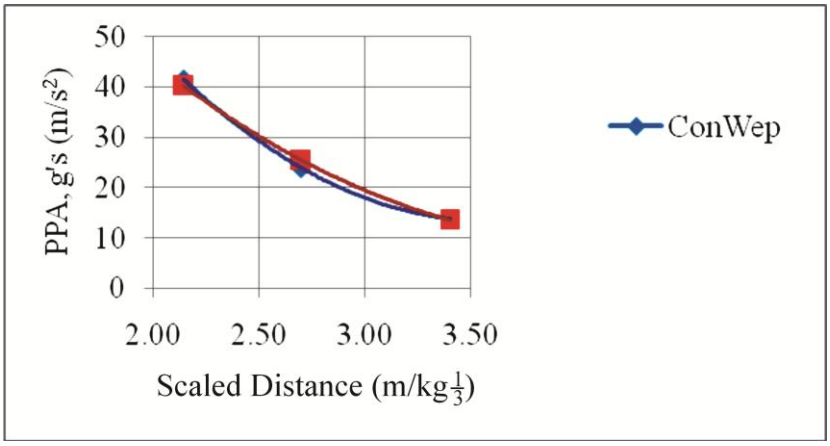

Figure 6: Comparison of ConWep Results with Experimental Output for PPA

Time of Arrival of the Ground Shock

The experimental values of time of arrival of the ground shock with respect to the scaled distance are shown in below table.

Table 8: Time of arrival of the Ground Shock ta

Explosive Weight (kg)	**Range (m)**	**Scaled Distance ($m/kg^{1/3}$)**	**t_a (msec)**
0.6	2.87	3.40	14.8
1.2	2.87	2.70	14.83
2.4	2.87	2.14	15.0

These values when plotted give the following empirical equation.

$$t_a = \frac{23.3}{C_s}\left(\frac{R}{Q^{1/3}}\right)^{-0.029}$$

Where t_a the ground shock arrival time in sec, R is the range in meters, Q s the TNT equivalent charge weight in kg and C_s is the soil seismic velocity which is taken as 1524m/s for the saturated sandy soil (soil considered for the current study).

Time Lag between Ground Shock and the Blast Wave Arrival Time

$$T_{lag} = T_a - t_a$$

$$T_{lag} = \frac{4.637}{C_a}\left(\frac{R}{Q^{1/3}}\right)^{-0.138} - \frac{23.3}{C_s}\left(\frac{R}{Q^{1/3}}\right)^{-0.029}$$

Structural Design of the RCC Wall

RCC wall is designed for blast loading using the methodology described in UFC_3_340_02. Calculation is shown below,

1. Establish design parameters

a). Refer to fig 4-17[1], maximum support rotation equal to 2 degrees and cross-section type I.

b). L = 100 inches, H = 80 inches

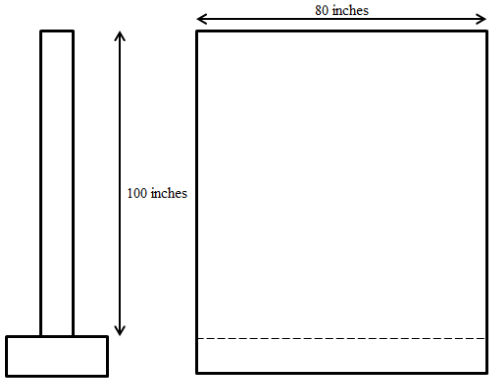

Figure 7: Wall Dimensions

c). Pressure-Time Loading

Charge Weight		= 4 kg
TNT Equivalent, Q		= 0.6 x 4 = 2.4 kg = 5.3 lb
Apply 20% safety factor, so Q		= 6.36 lb
Range, R		= 2.87 m = 9.416 ft
Scaled Distance, Z		= $\frac{R}{\sqrt[3]{Q}}$
=>	Z	= 5.08 ft/lb$^{1/3}$

Using fig 2-15[1], following values are interpreted

P_{so}		= 40 psi
$\frac{t_o}{Q^{1/3}}$		= 1.65 ms/lb$^{1/3}$
=>	t_o	= 3.05 ms

---

1. *UFC_3_340_02*

So, the pressure-time loading diagram will be as follows

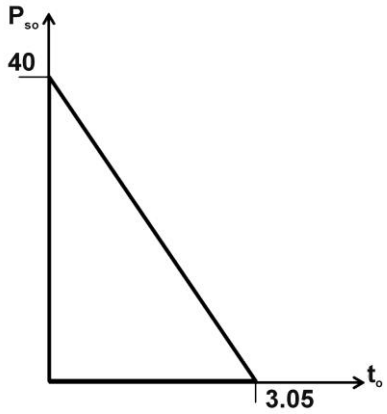

Figure 8: Blast Load

2. Select a cross-section of element including thickness and concrete cover over the reinforcement. Determine the static design stresses for concrete and the steel.

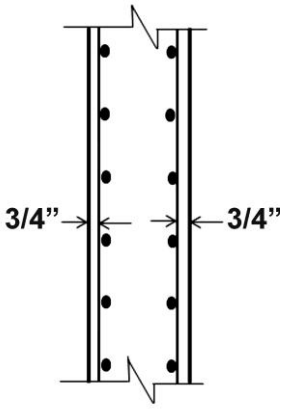

Figure 9: Reinforced Concrete Wall Cross-section

Assume wall thickness	T_c	= 6.5 inches
Concrete Cover		= ¾ inches

Static Stress of Concrete f'_c = 4000 psi
Static Stress of Reinforcement f_y = 50000 psi
3. Determine the dynamic increase factor for the concrete and steel using table 4-1[1]
Concrete:
Diagonal Tension = 1.00
Reinforcement:
Bending = 1.17

---

1. *UFC_3_340_02*

Diagonal Tension = 1.0
Direct shear = 1.10
4. Determine the dynamic strength of materials
Concrete (f'_{dc}):
Diagonal Tension 1.00 x 4000 = 4000 psi
Reinforcement (f_{dy}):
Bending 1.17 x 50000 = 58500 psi
Diagonal Tension 1.0 x 50000 = 50000 psi
Direct Shear 1.10 x 50000 = 55000 psi
5. Determine the dynamic design stresses using table 4-2[1]
Concrete (f'_{dc}):
Diagonal Tension = 4000 psi
Reinforcement ($f_{ds} = f_{dy}$ for $\theta < 2$):
Bending = 58500 psi
Diagonal Tension = 50000 psi
Direct Shear = 55000 psi
6. Assume Reinforcement in vertical direction = No.4 @ 8 in c/c
Assume Reinforcement in horizontal direction = No.4 @ 12 in c/c
7. Calculate d and the steel ratios for each direction.

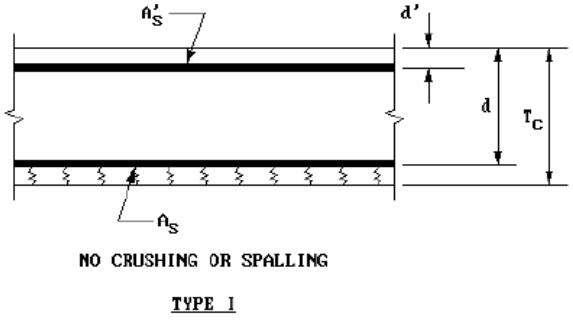

Figure 10: Type I Cross-Section

Let's assume No.3 stirrups.
d_V = 6.5 – 0.75 – 0.5/2 – 0.375
= 5.125 in

---

1. *UFC_3_340_02*

d_H = 6.5 – 0.75 - 0.5 – 0.375 – 0.5/2
= 4.625 in
ρ_V $= \frac{A_{sv}}{bd_v}$
$= \frac{0.29}{12 \times 5.125}$

$= 0.0047$

$\rho_H = \frac{A_{sH}}{bd_H} = \frac{0.20}{12 \times 4.625}$

$= 0.0036$

Use table 4-3[1] to calculate the minimum reinforcement ratios.

ρ_{min} in vertical direction $= \frac{1.875\sqrt{f_c}}{f_y} = \frac{1.875\sqrt{4000}}{50000}$

$= 0.0024$

Which is less than ρ_V so O.K.

ρ_{min} in horizontal direction $= \frac{1.25\sqrt{f_c}}{f_y} = \frac{1.25\sqrt{4000}}{50000}$

$= 0.0016$

Which is less than ρ_H so O.K.

8. Calculate the moment capacities of both the positive and negative reinforcement in both directions.

Use equation $M_u = \frac{A_s f_{ds}}{b}\left[d - \frac{a}{2}\right]$

In which $a = \frac{A_s f_{ds}}{0.85\, bf_{dc}}$

---

1. *UFC_3_340_02*

Now, moment in vertical direction

$M_{VN} = M_{VP} = \frac{0.29x58500}{12}\left(5.125 - \frac{0.29x58500}{0.85x12x4000}\right)$

$= 6660$ in-lbs/in

And moment in horizontal direction

$M_{HN} = M_{HP} = \frac{0.20x58500}{12}\left(4.625 - \frac{0.20x58500}{0.85x12x4000}\right)$

$= 4230$ in-lbs/in

9. Establish the values of r_u.

Using table 3-1[1]

$r_u = \frac{2M_N}{L^2} = \frac{2x6660}{(100)^2}$

$= 1.33$ psi

10. Determine the modulus of elasticity of concrete and steel

a). Modulus of elasticity of materials.

Modulus of elasticity of concrete $E_c = W_c^{1.5}\, 33(fc)^{1/2}$

$= (150)^{1.5}\, 33\, (4000)^{1/2}$

$= 3834250$ psi

Modulus of elasticity of steel $E_s = 29 \times 10^6$ psi

b). Modular Ratio.

Modular Ratio $n = \frac{E_s}{E_c}$

$= 7.5$

11. Determine the average moment of inertia for an inch strip.

a). Gross moment of inertia $I_g = \frac{T_c^3}{12}$

$= \frac{(6.5)^3}{12}$

---

1. *UFC_3_340_02*

$= 23\ in^4/in$

b). Moment of inertia of cracked section

Avg. depth for vertical direction, $d_{v(avg)} = 5.125$ in

Avg. depth for horizontal direction, $d_{H(avg)} = 4.625$ in

Avg. ρ in vertical direction, $\rho_{V(avg)} = \frac{A_s}{bd_{V(avg)}}$

$= 0.0047$

Avg. ρ in horizontal direction, $\rho_{H(avg)} = \frac{A_s}{bd_{H(avg)}}$

$= 0.0036$

Use fig 4-11[1], to find the coefficient of inertia of cracked section

Hence F for vertical direction $= 0.0246$

And F for horizontal direction $= 0.0193$

So, $I_{cV} = Fd_{V(avg)}^3$

$= 0.0246 \times 5.125^3$

$= 3.31\ in^4/in$

And $I_{cH} = Fd_{H(avg)}^3$

$= 0.0193 \times 4.625^3$

$= 1.91\ in^4/in$

c). Average moment of inertia of cracked section

$I_c = \frac{LI_{cV} + HI_{cH}}{L + H}$

$= \frac{(100x3.31) + (80x1.91)}{100 + 80}$

$= 2.69\ in^4/in$

d). Average moment of inertia $I_a = \frac{I_c + I_g}{2}$

$= 12.845\ in^4/in$

12. Establish the equivalent elastic stiffness

---

1. *UFC_3_340_02*

Using table 3-8[1], $K_E = \frac{8EI}{L^4}$

$= \frac{8x3834250x12.845}{(100)^4}$

$= 3.94$ psi/in

13. Establish the value of elastic deflection

$XE = \frac{r_u}{K_E}$

$X_E = \frac{1.33}{3.94}$

X_E = 0.338 in

14. Calculate the effective mass of element

a). Load mass factors

use table 3-12[1], Elastic K_{LM} = 0.65

Plastic K_{LM} = 0.66

Average load mass factor K_{LM} = 0.655

b). unit mass of an element $m = \frac{wT_c}{g}$

$= \frac{150x6.5}{32.2x12^3x12}$

= 0.00146 psi-sec^2/in

= 1460 psi-ms^2/in

c). Effective unit mass $m_e = K_{LM} \times m$

= 0.655 x 1460

= 956.3 psi-ms^2/in

15. Calculate the natural period of vibration.

$$TN = 2\pi\sqrt{\frac{m_e}{K_E}}$$

$$= 2\pi\sqrt{\frac{956.3}{3.94}}$$

---

1. *UFC_3_340_02*

= 97.9 ms

16. Determine the maximum response of element

a). Response Chart parameters:

Peak Pressure, P = 40 psi

Peak resistance, r_u = 1.33 psi

Duration of Blat load, T = 3.05 ms

Period of vibration T_N = 97.9 ms

P/r_u = 30

T/T_N = 0.03

b). using fig 3-64(a)[1]

X_m/X_E= 4.2

X_m = 4.2 x 0.338

= 1.42 in

17. Check the support rotation assumed.

Using table 3-5[1] X_m = Ltanθ

=> 1.42 = 100 x tanθ

=> tanθ = 0.0142

=> Θ = 0.81°

Which is less than 2° as assumed in step no.1. so assumed section is O.K.

18. Check diagonal tension at supports.

a). Calculate ultimate shear stress at support by dividing the values of the support shear from table 3-9[1].

So, $V_{uV} = \frac{r_u L}{d_v}$

$$= \frac{1.33x100}{5.125}$$
$$= 25.95 \text{ psi}$$

---

1. *UFC_3_340_02*

$$V_{uH} = \frac{r_u L}{d_H}$$
$$= \frac{1.33x100}{4.625}$$
$$= 28.75 \text{ psi}$$

b). Allowable shear stress

since $V_c = \left[1.9\sqrt{f_{dc}} + 2500\rho\right] \leq 3.5\sqrt{f_{dc}}$

so $V_{cV} = 1.9\sqrt{4000} + 2500 \text{ x } 0.0047$
$= 132 \text{ psi} \leq 3.5\sqrt{4000}$

$V_{cH} = 1.9\sqrt{4000} + 2500 \text{ x } 0.0036$
$= 129 \text{ psi} \leq 3.5\sqrt{4000}$

Since $V_{uV} < V_{cV}$

And $V_{uH} < V_{cH}$

So, the design of shear reinforcement will be based on the minimum requirement of the shear reinforcement.

Referring to table 4-4[1], for the case under consideration no stirrups are required.

Conclusions

1. If the horizontal range is kept constant, it is found experimentally that the numerical equation gives similar results as that provided by Brode and Henrych for small charge weights.
2. ConWep output and experimental values of peak pressure are in close agreement with each other.
3. For same horizontal range, larger the charge weight lesser will be the time of arrival of the shock wave.
4. For saturated sandy soil, the values of PPA obtained experimentally and analytically with ConWep are in close relation with each other.
5. The time lag between the ground shock and the blast wave shows that the air blast wave

---

1. *UFC_3_340_02*

reaches the structure before the arrival of ground shocks for small scaled distances say less than 5m.

6. The best economical solution for the blast resistant R.C.C structures is to maximize the stand-off distance for important buildings. As far as the structural design is concerned, the best approach is to prevent the progressive collapse.

References

[1] CONWEP, (1991), Conventional weapons calculations software based on TM 5-855-1, U.S. Army Engineers Waterways Station, 3909 Halls Ferry Road, Vicksburg, MS 39180.
[2] Brode. H.L, (1968), Review of nuclear weapons effects. Ann. Rev. Nucl. Sci. 18, pp 153-202.
[3] Brode. H.L. (1959), Blast wave from a spherical charge. Physics Fluids , 2: 217.
[4] Henrych J. (1979), The dynamics of explosion and its use. Elsevier, Amsterdam.

[5] Adeel. M (2010), “Blast Loading Effect on High Strength Reinforced Concrete Structure”. M.T thesis, University of Engineering and Technology, Taxila.

[6] Iqbal S.J. (2009), “Effects of an explosion on a concrete structure”. PhD thesis, University of Engineering and Technology, Taxila.

[7] Smith PD, Hetherington, JG (1994), “Blast and ballistic loading of structures”. Butterworth Heinemann.

[8] Structural Analysis Program, (2008) SAP2000 Advanced 12.0.1, Computers and Structures, Inc. University Ave. Berkeley, CA 94704,

[9] Technical Manual (TM-5-855-1). (1991), Fundamentals of protective design for conventional weapons. Headquarters, US Department of the Army, Washington, DC,

[10] UFC 3-340-02 (TM 5-1300). (2008), “Structures to Resist the Effects of Accidental Explosions”, U.S. Army Corps of Engineers,

[11] UFC 4-010-01. “DoD minimum antiterrorism standards for buildings”. (2007), U.S. Army Corps of Engineers.

[12] UFC 4-023-03. (2010), “Design of buildings to resist progressive collapse”. U.S. Army Corps of Engineers.

[13] Chengqing.W, Hao, H. March (2007), “Numerical simulation of structural response and damage to simultaneous ground shock and air blast loads”. International Journal of Impact engineering, Volume 34, Issue 3.

[14] Chengqing. W, Hao, H. July (2005), “Modeling of simultaneous ground shock and air blast pressure on nearby structures from surface explosions”. International Journal of Impact Engineering, Volume 31, Issue 6.

[15] Chengqing W., Hao H. July (2005), “Modeling of simultaneous ground shock and air blast pressure on nearby structures from surface explosions”. International Journal of Impact Engineering, Volume 31, Issue 6.

[16] Chengqing. W, Hao H, Lu. Y. February (2005), “Dynamic response and damage analysis of masonry structures and masonry infilled RC frames to blast ground motion”. Engineering Structures, Volume 27, Issue 3.

[17] Chengqin. W. Hao H. January (2005), “Numerical study of characteristics of underground blast induced surface ground motion and their effect on above-ground structures. Part I. Ground motion characteristics”. Soil Dynamics and Earthquake Engineering, Volume 25, Issue 1.

CNPP Fuel Rod Vibration Analysis Using Finite Element Method

Shakir Hussain[1], M. Rafique[2], Anwar Ahmad[3] and Syed Waseem Akhtar[4]

Abstract

The fuel rods in the PWR fuel assembly are continuously supported by spacer grids, which are located at intervals along the axial length of the fuel assembly. The coolant flow induces vibration in fuel rod which can wear away its cladding tube surface in contact with the support structure. Thus, it is important to examine the characteristics of the fuel rod vibrations. In the present study, two different methodologies have been developed to calculate the natural frequencies and mode shapes of the 300 MWe CNPP fuel rod. In the first methodology, a 2D planner flexure modal analysis of the fuel rod is performed using MATLAB software, while in the second, a 3D modal analysis is carried out using ANSYS software. In 3D analysis, actual geometry of the CNPP fuel rod and spacer grid spring/dimple support is modeled. The vibration analysis of pre-stressed model is carried out in the modal analysis module of ANSYS. The purpose of this study is not only to compare the 2D and 3D FE models but also to verify the results with the vibration measurements made by the Chinese for CNPP fuel rod. Both the 2D MATLAB and 3D ANSYS FE analyses results are found to be in good agreement with the Chinese test results and thus validate the analyses models.

Keywords: Fuel Rod, Spacer Grid, FE, Model Analysis, Natural Frequencies, Mode Shapes

Introduction

In a Pressurized Water Reactor (PWR), the fuel rods are supported at intervals along their lengths by spacer grids which maintain the lateral spacing between the rods. Each fuel rod is supported by six contact support points provided in each spacer grid (SG) cell by the combination of dimples and springs. The fuel rods are exposed to stringent operating conditions such as high temperature, high pressure and the massive coolant flow velocity (3~8m/s) during its designed lifetime (typically 3 cycles). The structural integrity of fuel rod cladding is very important being the first barrier to the release of radioactive fission products into the atmosphere.

The vibration of fuel rod is mainly generated by the high coolant flow which produces energy to induce vibrations. Since the coolant normally flows axially upward and parallel to the fuel rods, therefore, the vibration behavior of fuel rods is called axial flow-induced vibration (FIV). It is known that the vibration source in the reactor exists in wide range of 0 to 50 Hz Kenard M. W et al, (1995) which can make resonance causing potential damage to the fuel rod. Thus, it is important to understand the fuel rod vibration behavior in the reactor.

In order to prevent fuel failure due to the external excitation, the natural frequencies of the fuel rod are evaluated to assure that these are not matched with the expected excitation frequencies. These mechanisms must be prevented by adequate design of the fuel assembly structure (i.e., using an appropriate number of grid supports per fuel assembly and providing adequate stiffness) based on the coolant flow conditions in the reactor core. The principle design concern is not the prevention of the vibration mechanism but the limitation of resultant wear at the grid-to-rod support interface, which is produced due to relative motion (or sliding) between fuel rod cladding and SG.

The phenomena of fuel rod vibration have analyzed using FE analysis by various researchers. M.H Choi et al (2004) described the vibration analysis of continuously supported dummy fuel rod. H. S. Kang et al, Preumont. A, (1980) performed modal analysis for the newly designed SG. Comprehensive vibration behavior of PWR rods is studied by Andre Preumont Kang H. S. et al, (2001). Experimental study on vibration of flexible cylinders induced by axial flow is studied by M. P. Paidoussis Paidoussis M. P., (1968). However, it is still difficult to get the exact solutions for the fuel rod vibration supported by springs and dimples.

In the present study, a finite element (FE) model of the fuel rod has been developed to analyze vibration behavior of Chashma Nuclear Power Plant (CNPP) fuel rod. Two different FE models are adopted to calculate the modal parameters of the fuel rod. In first method FE based computer program

1-3 Directorate General Nuclear Power Fuel, Pakistan Atomic Energy Commission

is developed in MATLAB to calculate the eigenvalues and eigenvectors for the single fuel rod supported with eight SGs at intervals along its axial length. In this model, the fuel rod is replaced with 2D beam element and the SG dimples and springs are replaced with elastic spring elements. In the second method, a 3D modal analysis of the CNPP fuel rod is performed using ANSYS 13.0 software. The FE model of single fuel rod supported with eight SGs is generated as per actual geometry. Same material properties and boundary conditions are applied as in the previous case. For model validation, the results of both the analyses are also compared with the Chinese test results for CNPP fuel rod.

Description of Fuel Assembly

The CNPP fuel assembly consists of a 15×15 square array having 204 fuel rods, 20 guide thimbles, 1 instrumentation tube, 8 SGs, a bottom nozzle and a top nozzle. The fuel rod consists of slightly enriched uranium dioxide ceramic pellets contained in zircaloy-4 tubing which is plugged and seal welded at the ends to encapsulate the fuel. The guide thimbles and instrumentation tube in conjunction with 8 SGs and nozzles form the structural part, i.e. Skeleton, of the fuel assembly. The fuel rods are loaded into the skeleton such that there is clearance between the fuel rod ends and the top and bottom nozzles to accommodate irradiation induced growth and thermal expansion.

In the fuel assembly skeleton, the fuel rods are supported by SG springs and dimples. The main function of the SGs is not only to support the fuel rods at specific locations or intervals along their length but also to maintain the lateral spacing between the rods (rod to rod distance) throughout the designed life of the fuel assembly. In each SG cell, a fuel rod is supported by six contact support points (two springs and four dimples). The plane view of the fuel rod along with the isometric views of the SG contact arrangements with the fuel rod are shown in Figures 1 and 2, respectively.

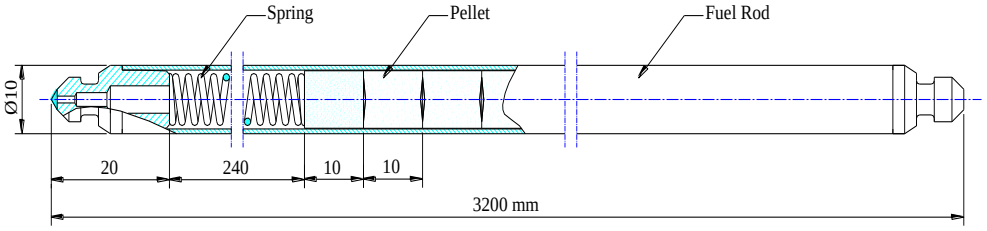

Figure 1: CNPP Fuel Rod

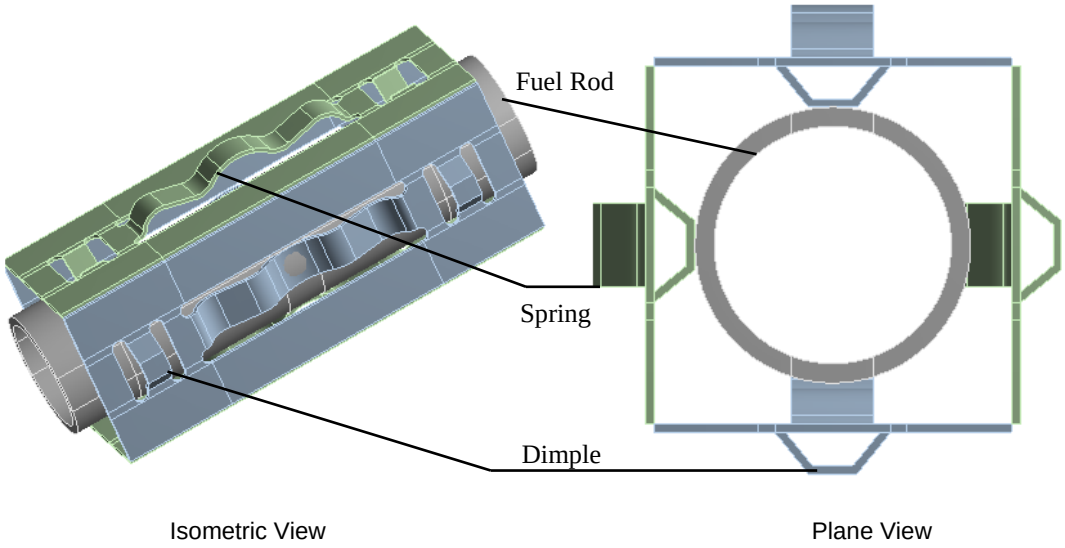

Figure 2: CNPP Spacer Grid Cell Showing the Contact Arrangements

FE Model and Analyses

In order to simplify the 2D & 3D models for determining the natural frequencies & modes shapes of the CNPP fuel rod, following assumptions are made:

i) During vibration, the fuel rod is always in contact with the springs and dimples of SG cell.

ii) The fuel stack does not contribute in the bending moment Kang H. S. et al, (2001).

iii) The mass per unit length includes both the cladding and fuel.

2-D Modal Analysis using MATLAB

In order to perform the 2D modal analysis using MATLAB software, it is assumed that the fuel rod exhibits only planner flexure vibration and its vibration plane is consistent with the plane determined by its supports structures, i.e. the springs and dimples in the SG cell are located in perpendicular planes to the fuel rod. The fuel rod is considered as 2D continuous beam element and the SG springs and dimples are replaced with 2D elastic spring elements with linear stiffness. Since, the CNPP fuel rod is supported by eight SGs, therefore, it can be regarded as seven span continuous beam Choi M. H. et al, (2004). The fuel rod is discretized in such a way that three nodes are taken at each SG cell (two at dimple and one at spring). Five nodes are taken in each span between two adjacent SGs; therefore, as a result 59 nodes are taken altogether in this continuous beam. The FE model of the CNPP fuel rod supported in a SG cell is shown in Figure 3.

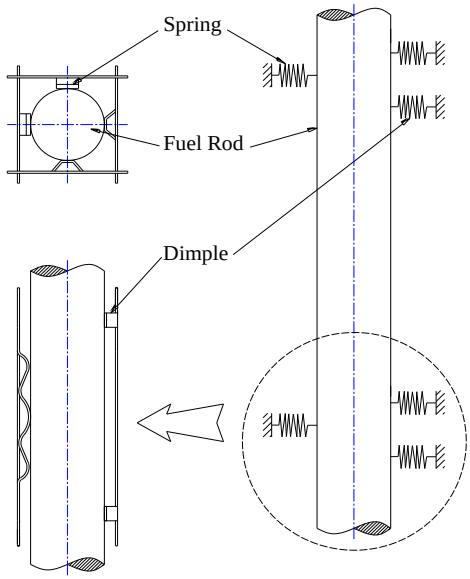

Figure 3: FE Model of CNPP Fuel Rod

Mathematical Model

The equation of the fuel rod vibration without damping is

$$[M]\{\ddot{X}\}+[K]\{X\}=0 \qquad \text{Eq. (1)}$$

Where $\{X\}=\{V_1,V_2,V_3,.....,V_n,\ \Phi_1,\Phi_2,\Phi_3,....\Phi_n\}^T$, $[M]$ is global mass matrix and $[K]$ is global stiffness matrix. Assuming displacement function;

$$\{X\}=\{U\}\{sin(wt+\Phi)\}$$

Simplifying Eq. (1) the terms

$$\{U\}sin(wt+\Phi)([K]-w^2[M])=0$$

$$[K]\{U\}-w^2[M]\{U\}=0 \qquad \text{Eq. (2)}$$

For the purpose of distinguishing the non-null mass term from the null mass term, vector $\{U\}$ is divided into two parts, i.e. $\{U\}=\{U_1,\ U_2\}^T$. Where, $\{U_1\}=\{\overline{V}_1,\ \overline{V}_2,\ \ldots.\ \overline{V}_n\}^T$ includes 'n' DoF (Degree of freedom) of non-null mass terms; and $\{U_2\}=\{\overline{\Phi}_1,\ \overline{\Phi}_2,\ \ldots\ \overline{\Phi}_n\}^T$ includes 'n' DoF of null mass terms. Correspondently, the stiffness matrix and mass matrix are divided into four parts respectively, i.e.

$$K=EI\begin{bmatrix}K_{11} & K_{12}\\ K_{21} & K_{22}\end{bmatrix} \text{ and } M=\begin{bmatrix}M_{11} & 0\\ 0 & 0\end{bmatrix}$$

Now the Eq (2) can be expressed as;

$$EI\begin{bmatrix}K_{11} & K_{12}\\ K_{21} & K_{22}\end{bmatrix}\begin{Bmatrix}U_1\\ U_2\end{Bmatrix}-w^2\begin{bmatrix}M_{11} & 0\\ 0 & 0\end{bmatrix}\begin{Bmatrix}U_1\\ U_2\end{Bmatrix}=0$$

Solving above equation

$$EI([K_{11}]\{U_1\}+[K_{12}]\{U_2\})-w^2[M_{11}]\{U_1\}=0 \qquad \text{Eq. (3)}$$

$$EI([K_{21}]\{U_1\}+[K_{22}]\{U_2\})-w^2(0)=0$$

$$\{U_2\}=-[K_{22}]^{-1}[K_{21}]\{U_1\}$$

Equation (3) becomes

$$EI\left([K_{11}]\{U_1\}+[K_{12}]\left(-[K_{22}]^{-1}[K_{21}]\{U_1\}\right)\right)-w^2[M_{11}]\{U_1\}=0$$

If $[\overline{K_{11}}]=[K_{11}]-[K_{12}][K_{22}]^{-1}[K_{21}]$

$$EI\left[\overline{K_{11}}\right]\{U_1\}=w^2[M_{11}]\{U_1\} \qquad \text{Eq. (4)}$$

The Eq. (4) represents the solution of general Eigen values. The matrix $[M_{11}]$ is symmetric and positive, the matrix $\left[\overline{K_{11}}\right]$ is real symmetric therefore, Cholesky method is adopted for analysis. Decompose $[M_{11}]$ into two triangular matrices, i.e. $[M_{11}]=[L][L]^T$, Where $[L]$ is an upper triangular matrix. Since $[M_{11}]$ is a diagonal matrix.

$$[L]=\begin{bmatrix}M_{11}^{1/2} & & & 0\\ & M_{22}^{1/2} & & \\ & & , & \\ & & , & \\ 0 & & & M_{nn}^{1/2}\end{bmatrix}=[M_{11}]^{1/2}$$

Then assuming that $\{U_1\}=[M_{11}]^{-1/2}\{Z\}$

Putting value of $\{U_1\}$ in Eq. (4)

$$EI\left[\overline{K_{11}}\right][M_{11}]^{-1/2}\{Z\}=w^2[M_{11}][M_{11}]^{-1/2}\{Z\}$$

$$EI\left[\overline{K_{11}}\right][M_{11}]^{-1/2}\{Z\}[M_{11}]^{-1/2}=w^2\{Z\}$$

$$A = EI\left[\overline{K_{11}}\right][M_{11}]^{-1/2}[M_{11}]^{-1/2}$$

$$A\{Z\} = W^2\{Z\} \qquad \text{Eq. (5)}$$

Here, the matrix $[A]$ is a real symmetric matrix and the Eq. (5) is a solution of eigenvalues and eigenvectors. Finally, the vibration modes are normalized, i.e. $\{U_i\}^T[M_{11}]\{U_i\}=1$. A Schematic of the complete solution methodology is given in Figure 4.

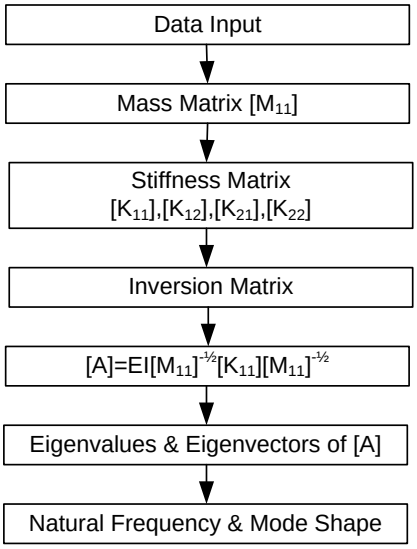

Figure 4: Model Flow Diagram

Stiffness Matrix

The fuel rod is discretized with beam element. Since the distance between the neighboring springs is only 1~2 times larger than the outside diameter of the fuel rod, therefore shear deformation of the beam is considered while calculating deflections and rotations of the beam. For this reason short beam elements (line elements) are used when using the FE method to calculate the fuel rod natural frequencies. It has six degrees of freedom (DoF) at each node, which includes translations and rotations along the x, y, and z directions, respectively. The stiffness matrix of the short beam element can be expressed as;

$$[K]_{l_i}^e = \frac{EI}{(1+b_i)\,l_i}\begin{bmatrix} 12 & 6l_i & -12 & 6l_i \\ 6l_i & (4+b_i)l_i^2 & -6l_i & (2-b_i)l_i^2 \\ -12 & -6l_i & 12 & -6l_i \\ 6l_i & (2-b_i)l_i^2 & -6l_i & (4+b_i)l_i^2 \end{bmatrix} \qquad \text{Eq. (6)}$$

Where

$[K]_{li}^e$ Stiffness matrix of the beam element,

l_i. Span length of beam element

E Young's modulus of elasticity for fuel rod

$$bi = \frac{12kEI}{GAl_i}$$

I Inertia moment of the beam cross section

G Shear elastic modulus of the fuel rod

A Cross section area of the beam element

k Co-efficient due to non-uniform distributed shear stress on the beam cross section

The stiffness matrix represents a beam element, which is under pure bending load (no axial or torsion loads). Nodal displacements and nodal moment are related as:

$$\begin{bmatrix} V_i \\ M_i \\ V_{i+1} \\ M_{i+1} \end{bmatrix} = [K]^e_{l_i} \begin{bmatrix} v_i \\ \Phi_i \\ v_{i+1} \\ \Phi_{i+1} \end{bmatrix}$$

Where V_i , v_i are the nodal displacements of the *i*-the node, M_{i+1}, Φ_i are respectively the nodal moment and rotation of the *i*-th node etc. generalized equation for the continuous beam is as follows;

$$\{P_1, \ P_2, \ .. \ P_n, \ M_1, \ M_2, \ ... \ M_n\}^T =$$

$$[K]\{V_1, \ V_2, \ ..... \ V_n, \ \Phi_1, \ \Phi_2, \ ..... \ \Phi_n\}^T$$

Where, the matrix $[K]$ is a global stiffness matrix and "P" and "M"are external nodal force and nodal moment. Expressions for all elements of the Global stiffness matrix are obtained after collecting and arranging all the nodal equilibrium equations.

Mass Matrix

A lumped mass technique is adopted which is a simpler method of approximation to replace the distributed inertia of the continuous system by a finite number of lumped inertia elements. All inertia effects are concentrated at the nodes. The nodes are assumed to be connected by elastic but mass less elements. Here rotational inertia terms in the mass matrix are omitted and hence the mass matrix is reduced to the form;

$$M = \begin{bmatrix} M_{11} & & & 0 \\ & M_{22} & & \\ & & , & \\ & & & M_{nn} \\ 0 & & & 0 \end{bmatrix}$$

Where; $M_{11} = \frac{1}{2} m_1 l_1$, $M_{nn} = \frac{1}{2} m_{n-1} l_{n-1}$

$M_{ii} = \frac{1}{2}(m_{i-1} l_{i-1} + m_i l_i)$ and $(i = 2,3,...n-1)$

As described in the previous section that fuel stack will not contribute in bending moment because fuel stack is not a single intact part, it is divided into small fuel pallets which will not resist the bending of fuel rod. Therefore, bending moment and modulus of elasticity of fuel cladding is only considered for modal analysis. Input variable for calculation of modal analysis are given in Table 1.

Table1. Input Variable

Variable Name	Value
Elastic module of the fuel rod cladding material	1.02×10^{11} N/m^2
Shearing modulus of the fuel rod cladding material	3.57×10^{10} N/m^2
Moment of inertia of the fuel rod cladding cross section	2.22×10^{-10} m^4
Outer diameter of the fuel rod	0.01 m

Inner diameter of the fuel rod	0.0086 m
SG dimple stiffness	490 kN/m
SG spring stiffness	32.2 kN/m

The normal deflection curve, which determines the stiffness ratio (listed in Table 1) of the SG spring and dimple are shown in Figure 5. The results reveals that stiffness ratio of the dimple is much higher than the spring. It is also evident that dimple deflection curve is linear while spring deflection curve is non linear. This nonlinearity cannot be incorporated in free modal analysis.

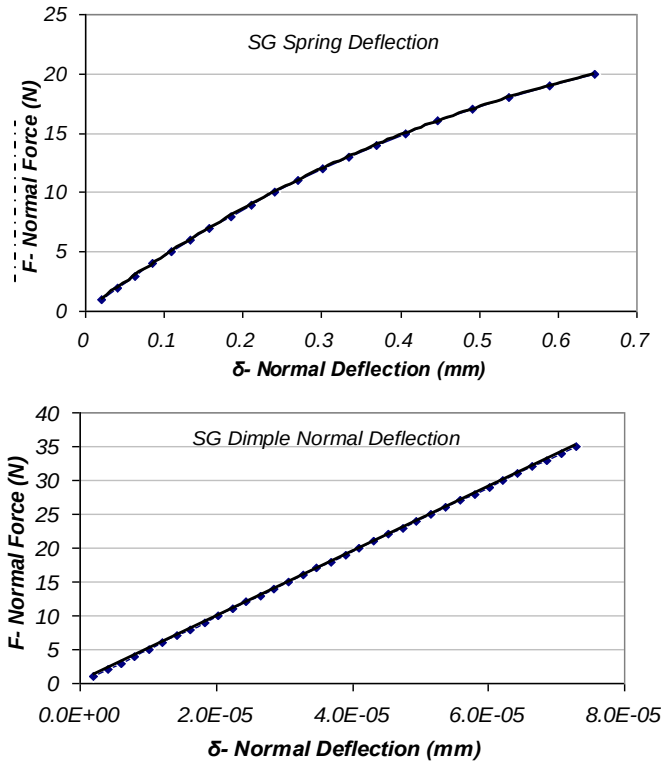

Figure 5: SG Spring & Dimple Deflection Curves

Therefore, the stiffness ratio of spring at 0.4 mm deflection is taken for analysis, which is initial deflection of the spring when fuel rod is inserted in the SG of fuel assembly.

Eigen Values and Eigen Vectors

Eigen values (Natural frequencies) and eigenvectors (mode shapes) of the fuel rod are calculated through solving the governing equations. Material and mechanical properties of the fuel rod and SG are attributed according to values listed in Table 1. The first six natural frequencies are listed in Table 2.

Table2. Natural Frequencies Fuel Rod using MATLAB

Mode	***Natural Frequency***
1st	*56.53*
2nd	*62.01*
3rd	*68.91*
4th	*77.98*
5th	*87.74*
6th	*95.97*

The normalized mode shapes with correspondent natural frequencies are given in Figure 6.

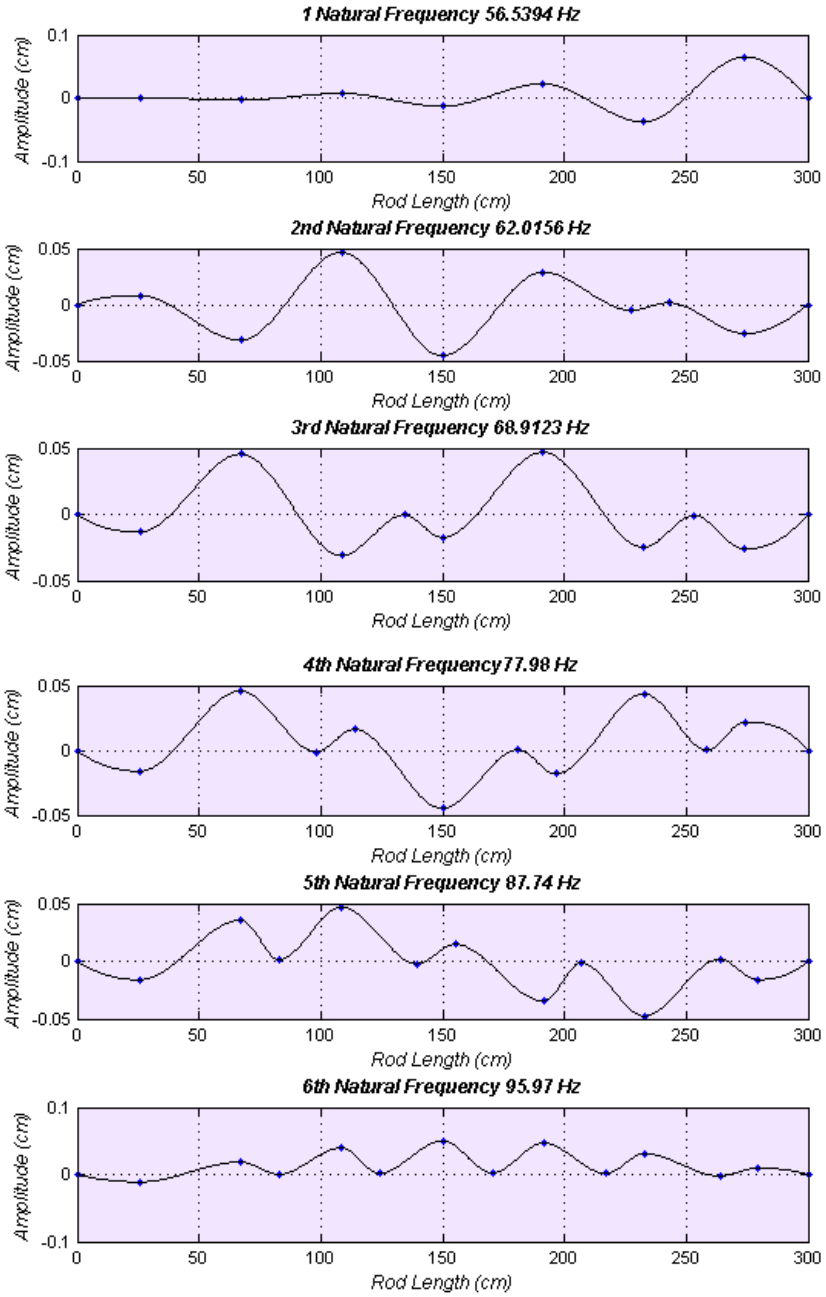

Figure 6: Mode Shape of CNPP Fuel Rod

3-D Modal analysis using ANSYS

3D modal analysis of CNPP fuel rod is also performed using ANSYS in order to find out the natural frequencies and mode shape. The methodology is consist of two steps first contact analysis is performed between the fuel rod and SG in ANSYS structural analysis module and then pre-stress vibration analysis is performed using the ANSYS modal analysis module.

Contact Analysis

Fuel rod is interferencely fitted between the SG spring and dimple. The vertical distance between the outer surface of the spring and opposite dimple is 9.6 mm and fuel rod outer diameter is 10mm. when the fuel rod is inserted between the SG it will deform 0.4mm in normal direction. In order to establish the frictional contact between the fuel rod and SG springs and dimples nonlinear contact analysis is performed.

In this regard 3-D solid modeling of CNPP SG cells and fuel rod is created in ANSYS design modeler as per actual geometry. It is described in the previous section that fuel section doesn't contribute the bending moment therefore cladding of the fuel rod is modeled in ANSYS but mass of the fuel pellet is added in the cladding mass. All the material and mechanical properties are attributed in accordance with material and geometry of the SG and fuel rod, as listed in table 3. As a boundary condition the SG is constrained from right and left side (along the fuel rod axis) for all directional and rotational movements. Model is meshed with 'Solid-186' element and symmetric contact pair is created between fuel rod and SG at six points in SG cell (two at SG spring and four at SG dimple) with contact element 'Conta-174' and 'Targe-170'. Contact arrangement of two SG straps (upper and lower) in a single cell is shown in Figure 7.

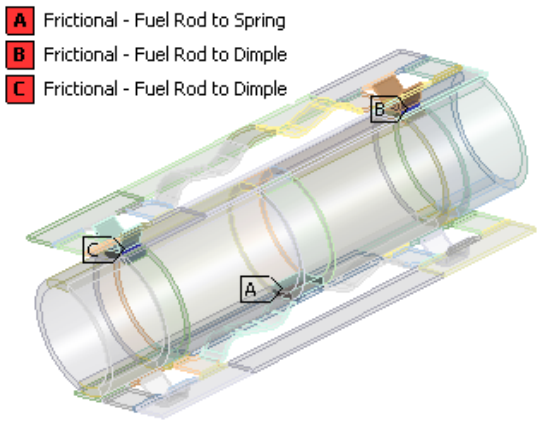

Figure 7: Contact Point in SG Cell

Same methodology is adopted for all eight SG cells along the fuel rod. A brief summary of FE model is given in given in Table 3.

Table3. ANSYS FE Model Summary

Element type for SG cell and fuel rod	Solid-186
Contact/Target element	Conta-174, Targe-170
Number of elements of 'Solid-186'	15502
Number of elements of 'Conta-174'	1073
Number of elements of solid 'Targe-170'	455
Contact type	Frictional
Contact formulation	Augmented Lagrange
Modulus of elasticity of SG spring	2.0×10^5 MPa
Elastic modulus of the fuel rod cladding	1.02×10^5 MPa
Shearing modulus of the fuel rod cladding	3.567×104 MPa
Coefficient of friction	0.3

After contact analysis is performed, it is found that the spring is deformed only 0.38 mm (~0.4 mm) in normal direction, whereas the dimple deflection is almost negligible. The reason is that the normal stiffness of the SG dimple is much higher than the normal stiffness of SG dimple. Therefore, SG dimple is showing the rigid body motion behavior.

Figure 8 shows the front sectional view of the meshed fuel rod in contact with the SG spring. Before contact analysis spring is 0.4 mm inside the fuel rod but after contact analysis spring is deformed and adjusted to touch condition with fuel rod outer surface. Same contact creation is achieved for all contact pairs along the fuel rod.

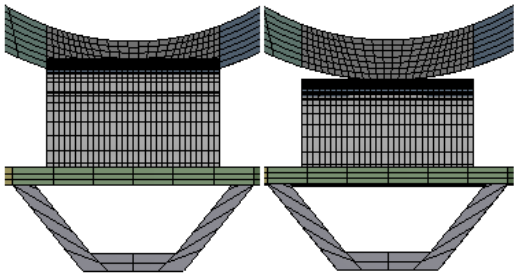

Figure 8: SG Spring Deformation

Pre-stressed Modal Analysis

Modal Analysis of fuel rod is performed after creating the contact between fuel rod SG. As a boundary condition SG axial edges along the fuel rod are constrained from all movements in all direction. Fuel rod is constrained to move in axial direction. Natural frequencies and mode shapes are extracted using Lanczos method.

Natural Frequencies and Mode Shapes

The first six mode shapes of CNPP fuel rod with corresponding calculated natural frequencies are shown in Figure 9.

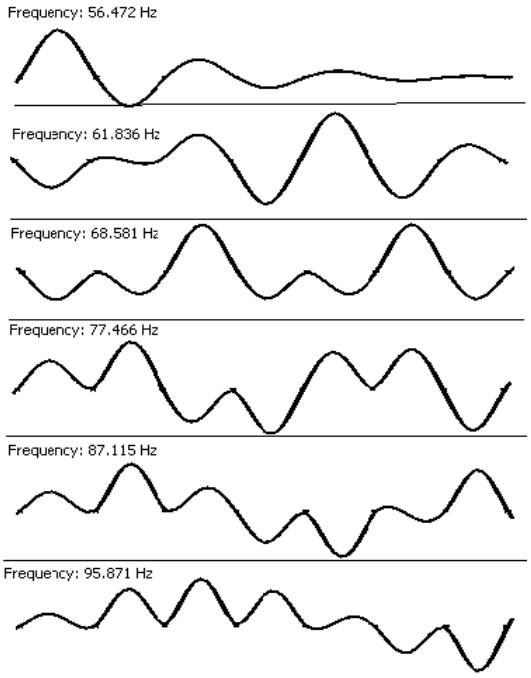

Figure 9: Fuel Rod Mode Shape using ANSYS

Comparison with Test Results

The mode shapes and natural frequencies of CNPP fuel rod calculated through MATLAB and ANSYS FE analyses have been compared with the test results conducted by Chinese A18.21 – 1994 "A Computer Code for the Calculation of Natural Frequencies and Modes of Fuel Rod Vibration Specifications". The comparison of results is listed in Table5 which depicts that analytical FE modal results are in good agreement with test results. Mode shapes obtained from both the analyses are also shows same pattern.

Table5. Natural Frequencies comparison

Mode	**Natural Frequencies (Hz)**		
	MATLAB	ANSYS	CHINESE TEST
1st	56.53	56.5	57.9
2nd	62.01	61.8	63.7
3rd	68.91	68.6	67.7
4th	77.98	77.5	78.3
5th	87.74	87.1	92.3
6th	95.97	95.9	99.8

Conclusions

Results obtained from the 2-D modal analysis accords with the 3-D ANSYS analysis and their concurrence with the Chinese test result enhanced the confidence in the FE analysis.

1) Fuel rod fundamental natural frequency is 56 Hz, which is higher than the expected excitation frequencies in the reactor (i.e., 0 to 50Hz), Kenard M. W et al, (1995).
2) Number of SG per fuel assembly and its stiffness has a significant effect on the modal parameters of fuel rod. The same conclusion was drawn by Kang H.S. et al (2000).
3) Increasing the number of SGs in a fuel assembly will decrease vibration amplitude of fuel rod because unsupported length of fuel rod will decrease and make fuel rod boundary conditions more stiffer. However, this will affect thermal hydraulic parameters and SG stiffness is the only parameter which controls the design of SG.

References

[1] Kenard M. W et al, (1995) "A Study of Grid-to-Rod Fretting Wear in PWR Fuel Assemblies", Vol. 1 S. M Stoller Co.

[2] Choi M. H. et al, (2004) "Vibration Analysis of Dummy Fuel Rod Continuously Supported by Spacer Grids", NED, Vol. 234, pp 185-196.

[3] Preumont. A, (1980) "on the Vibrational Behavior of Pressurized Water Reactor Fuel Rods Nuclear Fuels",

[4] Kang H. S. et al, (2001) "Modal Analysis of PWR Fuel Rod Supported by the Newly Designed Spacer Grid", Transaction, SMiRT 16, Washington DC,

[5] Paidoussis M. P., (1968) "An Experimental Study of the Vibration of Flexible Cylinders Induced by Axial Flow", Trans. of ANS, 11, 352p,

[6] A18.21 – 1994 "A Computer Code for the Calculation of Natural Frequencies and Modes of Fuel Rod Vibration Specifications", CNPP ToT document, SNERDI China.

[7] Kang H. S. et al, (2000) Verification Test and Model Updating for a Nuclear Fuel Rod with its Supporting Structure, Journal of Korean Nuclear Society,.

A Methodology for Determining Grid-to-Rod Fretting Wear of CNPP Fuel Rods

Muhammad Rafique[1], Shakir Hussain[2], Anwar Ahmad[3], Muhammad Omair Khan[4] and Syed Waseem Akhtar[5]

Abstract

The grid-to-rod fretting wear methodology is developed based on Archard wear equation to calculate the cladding wear depth of CNPP fuel rod during its residence time within the reactor core. This methodology is coupled with FRV, FRPV, FRCB and ANSYS computer codes to determine the input parameters such as residual spacer grid spring force, effective sliding distance, cladding creep down, RMS displacement at dimple location, and initial hold-down force of the spacer grid spring etc. of wear equation. After determining all these parameters, the wear depth of CNPP fuel rod due to FIV (considering the effects of thermal expansion, cladding creep and irradiation induced spring relaxation) is calculated to be about 9.5 µm which is less than the design criterion (i.e., 10 % of the Zircaloy-4 cladding tube wall thickness, 70 µm at the end of life). In case of CNPP, for an initial spring force of 14.5 N the slippage of fuel rod occurs when the spacer grid spring relaxation caused by irradiation reaches to 76%.Based on these results, it is expected that the fretting wear depth of CNPP fuel rod will remain within the acceptable limits during its entire lifetime.

Keywords: Fuel Rod, Spacer Grid, Spring Relaxation, FIV, RMS, Fretting Wear Depth, EOL

Introduction

In Pressurized Water Reactors (PWRs), the nuclear fuel rods consist of slightly enriched UO_2 ceramic pellets contained in Zircaloy-4 tubing which are plugged and seal welded at the ends to encapsulate the fuel meat. The fuel rods are loaded into the skeleton so that there is a clearance between the fuel rod ends and the top and bottom nozzles to accommodate the effects of thermal expansion and irradiation induced growth. Within a fuel assembly, the fuel rods are supported by the spacer grids located at intervals along the axial direction which also maintain the lateral spacing between the rods (rod pitch) throughout the designed lifetime. In each grid cell, a fuel rod is supported by six contact support points (two springs and four dimples) provided in the orthogonal directions. The dimples and springs, being the key elements of the spacer grid cell, play a major role as the support system of the fuel rods. The springs provide elastic support, whereas, dimples provide rigid support to the fuel rod. The magnitude of the supporting force provided by the grid cell is set high enough to minimize the fretting wear of the fuel rods at the end of life (EOL), without overstressing the cladding surface at the contact points. The contact arrangements of the spacer grid with the fuel rod are shown in Figure 1.

At reactor operating conditions, these fuel rods are subjected to turbulent excitation exerted by the coolant flowing parallel to their axes. The flowing coolant produces energy to induce vibrations, known as flow induced vibration (FIV), in the fuel rods. The fuel rods FIV phenomena have been studied by several researchers. Wambsganss and Chen S.S. (1971) studied FIV by considering a cylinder simply or elastically supported at both ends. However, they were unable to model the specific effects of forces, produced at the spring/dimple supports similar to the actual fuel rods. The FIV problem was also studied by Burgreen D. et al (1958), Quinn E.P. (1962), Sogreah H. (1962), Pavlicaand Marshall R.C (1965), Paidoussis M. P., (1968) and Morris A. E (1964) . Burgreenet al gave the earliest correlation for determining the vibration amplitudes of the fuel rod. Paidoussis extended the work of Burgreen et al and published a revised correlation for the fuel rod vibration amplitude. Kang et al (2001) proposed an analytical model of FIV for a rod supported by two translational springs at both ends. Since the high coolant flow is inevitable for reactor heat transfer, therefore, it is impossible to control or restrain the fretting wear phenomena induced by FIV within the reactor core.

1-3 Directorate General Nuclear Power Fuel, Pakistan Atomic Energy Commission,

At the beginning of life (BOL), the frictional forces within the spacer grid cell of fuel assembly are set sufficiently high enough to limit the relative motion between the fuel rods and the springs/dimples induced by FIV. However, due to the spacer grid spring relaxation with increase in burn up and cladding creep down, a clearance may emerge between the grid and the fuel rods, which changes the grid-to-rod contact conditions. Therefore, flow-induced vibrations (FIV) caused by turbulence coupled with the spring relaxation may lead to fretting wear of fuel rods. If the tube is perforated as a result of severe wear damage, radioactive fission gases are released into the primary heat transport system. As a result the radioactivity level exceeds the regulatory limits, the condition which is not preferred by the utilities.

Primarily, there are three types of wear mechanisms caused by FIV namely: i) impact wear, ii) fretting wear and iii) sliding wear. The impact wear is associated with very large vibrations amplitude leading to rapid fuel failure. Whereas, the fretting and sliding wears are typically related to relatively smaller vibration amplitudes. It results from the combined action of rubbing and tapping between the fuel rod and its support structure within the spacer grid cell. Actually, the slippage of the fuel rod within the spacer grid cell is allowed by the designer to accommodate the irradiation and thermal expansion effects. However, such movement of the fuel rod is restricted from top and bottom ends (i.e. by top and bottom nozzles). Consequently, the fretting wear is largely caused by the rotation or motion of the fuel rod inside the grid cell in horizontal plane. Whereas, the sliding wear occurs only by rubbing or sliding motion between the grid support and fuel rod cladding tube. Nevertheless, it is very difficult to distinguish between these later two types of wear mechanisms Perumont A, Sep (1982), Kim Y. H., et al, Aug, (1997), Shuffler C.A, (2004), Tong L. S. and Weisman J., (1996).

The fretting wear is one of the most common causes of fuel failures in PWRs which may shorten the lifetime of the fuel rods which are designed for 3–5 years. The factors, which predominantly affect the fretting wear of fuel rod include the spacer grid spring force, area of contact surfaces, temperature at support points, coolant flow velocity, grid growth, reduction in rod diameter due to cladding creep down, water chemistry, etc. Among these, the spacer grid spring force is the key parameter which has a crucial impact on the grid-to-rod fretting tendency during the in-reactor lifetime of the fuel. Moreover, the fuel assembly bow and formation of oxide layer on the contact surfaces also contribute to alter the grid-rod support conditions Rubiolo P. R. and Young M., (2009). In short, due to involving multi-variables and uncertainties associated with the fuel assembly mechanical properties and reactor parameters, the analytical prediction of the fretting-wear damage of a PWR fuel rod is a complex problem. No general solution of fretting wear problem covering all aspects can be found in spite of its importance. Resultantly, the most effective method of investigating such complex problems is to combine the computational methods with the experimental studies.

In this study, a simple grid-to-rod fretting wear (GTRF) methodology based on the Archard Wear Theory Kim Y. H., et al, Aug, (1997) is developed to calculate the wear depth of the CNPP fuel rod for its designed life time mainly from mechanical viewpoint. In order to determine various input parameters, this methodology is coupled with FRV, FRPV, FRCB and ANSYS computer codes. Based on these analyses, the results for onset of fuel rod slippage, effective sliding distance and fretting wear volume / depth have been presented for the case of 300 MWeCNPP fuel rod.

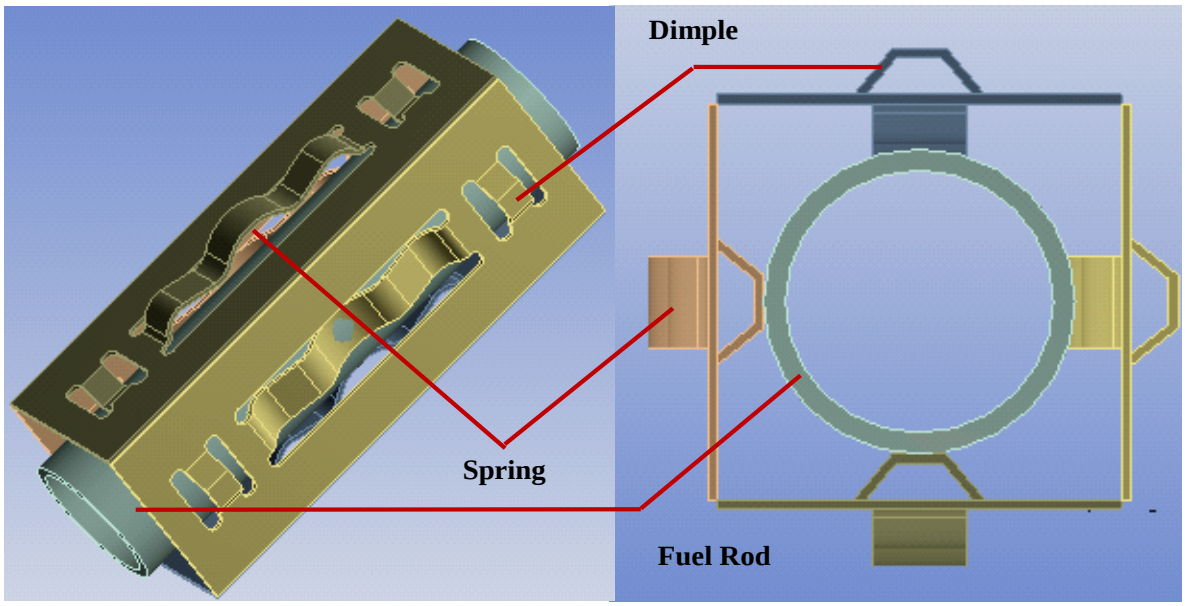

Figure 1: CNPP Spacer Grid Cell Showing the Grid-to-Rod Contact Arrangements

Design Criterion

The frictional force provided by the springs and dimples within the spacer grid cell shall provide sufficient support to limit the fuel rod vibration throughout the designed life-time and to maintain cladding fretting wear within acceptable limit. The cumulative fuel rod cladding wear depth due to fretting, fatigue, thermal expansion, oxidation, creep and irradiation induced growth should be less than 10% of the wall thickness of the cladding at EOL (i.e. <70 μm for CNPP fuel rod) Chashma Nuclear Power Plant Unit-2, Final Safety Analysis Report (FSAR), Mar (2009).

Calculation Methodology

The overall methodology used to calculate the fretting wear depth of the fuel rod is shown in Figure 2 Kim Y. H., et al, Aug, (1997).

The methodology developed , based on the concept of Archard wear theory, provides a good relationship to estimate the wear volume of fuel rod during its residence time within the reactor core at its operating conditions. For this purpose, the Equations 1, 2 and 3, explained in the proceeding sections, are used to estimate the wear volume of CNPP fuel rod. These calculations are coupled with FRV, FRPV, FRCB and ANSYS computer codes to determine various input parameters for solving these equations.

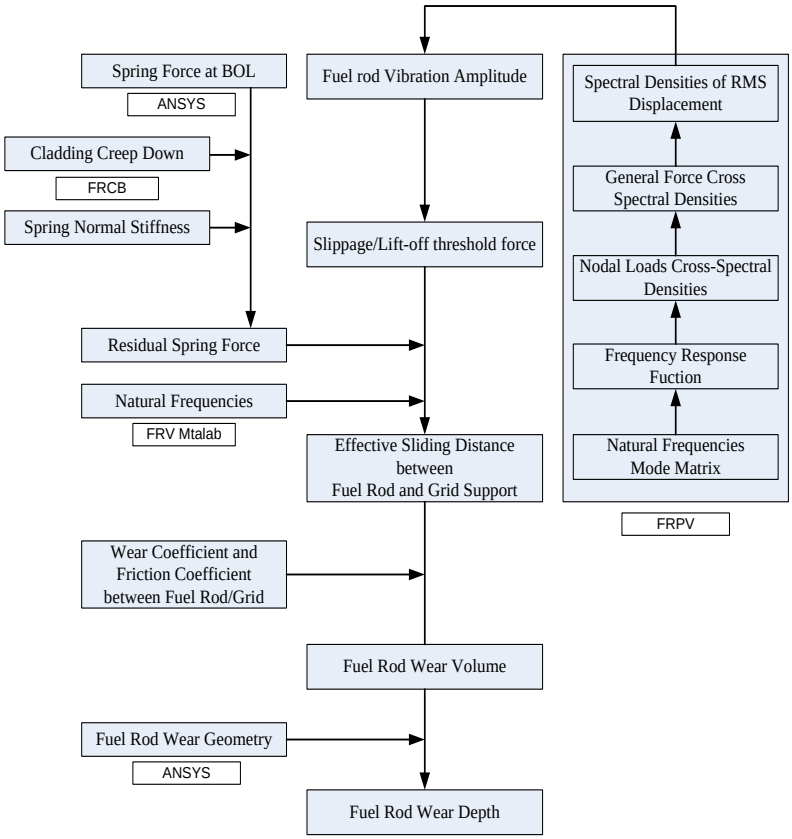

Figure 2: Flow Chart for Calculating the Fretting Wear Depth of Fuel Rod

Wear Volume

The wear volume of the CNPP fuel rod is calculated using the ArchardWear Equation which was based on the following assumptions [10]:

i) The wear volume (V) produced due to effective sliding distance (L) is proportional to the contact area.

ii) True area of contact is formed by the local plastic deformation of spacer grid spring.

iii) The material particles removed by sliding or rubbing motion are hemispherical and have same diameter.

In this model, the fretting wear volume of fuel rod produced as a result of FIV is related to the residual spring force and the effective sliding distance by the following expression:

$$V = \frac{SF_S L}{3H} \qquad (1)$$

Where

V = Wear volume (mm^3)

S = Wear coefficient (-)

F_s= Residual spring force on contact surfaces (N)

L = Effective or accumulative sliding distance (mm)

H = Material hardness (N/mm^2)

The numerical constant 3 in Equation 1 covers the shape factor. This equation is used not only to determine the fretting wear volume (*V*) but also to estimate the onset of fuel rod slippage within the spacer grid cell. Usually, wear coefficient (*S*) and hardness (*H*) of Zircaloy is determined experimentally. However, in the absence of such data, the values of these coefficients are taken from the literature. Whereas, the determinations of residual spring force (F_s), effective sliding distance (*L*) and other parameters are described below.

Residual Spring Force

During reactor operation, with the increase in fuel burn up (fluence) spacer grid spring force relaxation and cladding creep down takes place as a result of neutron irradiation. The values of residual spring force of the grid material(Inconel 718) after a fast fluence of 0.85×10^{21} n/cm^2 and 2.5×10^{21} n/cm^{2}arereported to be about 1/3rdand 1/7th, respectively, of their initial values Tong L. S. and Weisman J., (1996).Thus, for the case of CNPP, it is believed that the spring relaxation at EOL is about 80% or more for the central spacer grids that are exposed to the maximum fast neutron flux. Whereas, for the case of top and bottom spacer grids, the spring force relaxation at EOL is expected to be around60 % of the initial value. Therefore, the initial spring force needs to be set substantially higher to provide sufficient safety margin for the minimum hold-down force required at EOL.

The residual spring force is determined taking into consideration the parameters which influence the spring force relaxation during the reactor operation. These include: initial spring force, irradiation induced spring force relaxation, cladding creep down and thermal expansion. The residual spring force (F_s) is calculated by the formula:

$$F_s = (F_{BOL} - KC)(1 - R) \qquad (2)$$

Where

F_s=Residual spring force (N)

F_{BOL} = Spring force at BOL (N), calculated with the help of ANSYS from contact analysis

K = Initial spring stiffness (N/m)

C = Cladding creep down (mm), calculated from FRCB code

R= Spring force relaxation (%)

Effective Sliding Distance

The effective sliding distance is the overall distance caused by slippage of fuel rod both in axial and transverse directions. The slippage of fuel rod within the spacer grid cell is allowed not only to overcome the creep bowing effects but also to limit the stresses produced due to thermal expansion and irradiation growth of the fuel rod. The phenomenon of slippage between the cladding tube and the grid springs/dimples is initiated when the tangential force produced by FIV exceeds the frictional force of spacer grid springs. The spacer grid spring and dimples are designed in such a way that the resulting spring force is neither too high nor too low. If too high, it may lead to fuel rod creep bowing. If too low, it will cause fretting wear failure of fuel rod. Thus, the spacer grid spring force is the most important parameter to avoid such problems. The effective sliding distance L at a dimple location during fuel rod residence time t is related to the frictional force of spacer grid spring by the following relationship:

$$L = 4 f_n t\left(Y_{dn} - \frac{F_S . \mu}{2 K_{dt}} \right) \qquad (3)$$

Where

L = Effective sliding distance (m)

f_n =Fuel rod vibration frequency of nth mode (Hz), determined from FRV

t = Fuel rod residence time (sec) within the reactor

Y_{dn} = Maximum RMS displacement at dimple location (m)

F_s = Residual spring force (N)

K_{dt} =Dimple tangential stiffness (N/m), experimental value from literature

μ =Co-efficient of friction between fuel rod and spacer grid

In Equation 3,'Y_{dn}' is the RMS displacement of fuel rod produced by the FIV at dimple location and $F_s.\mu/2K_{dt}$ is the dimple displacement in tangential direction. Thus, the factor $\left(Y_{dn} - F_S.\mu / 2K_{dt}\right)$ in Equation 3 is the relative motion between fuel rod and the spacer grid dimple. This relative motion occurs when Y_{dn} becomes greater than $F_s.\mu/2K_{dt}$ resulting in fretting wear of the fuel rod cladding at the grid-rod contact points.

Input Parameters Calculations

First of all, creep, contact, modal and FIV analyses of CNPP fuel rod have been performed to determine the input parameters of Equations 1-3. These studies involved the execution of computer codes such as FRV, FRPV, FRCB and ANSYS. The computer codes FRPV (fuel rod vibration analysis under parallel flow) and FRV (fuel rod vibration model analysis) are executed to determine the RMS displacement at dimple location, natural frequencies and mode shapes of the fuel rod F2.6, A Computer Code, FRV, (1994), A18.21, A Computer Code, FRV (1994). FIV analysis of CNPP fuel rod is carried out for a flow velocity of 3.4 m/s considering 0.3% damping to calculate the maximum RMS displacement at the dimple location. The computer code FRCB (fuel rod creep bowing) is used to calculate the cladding creep down A18.22, Oct (1993). The effects of temperature and neutron flux on the cladding creep down are also considered in these calculations. Contact analyses of fuel rod have been performed using ANSYS Workbench structural module ANSYS Release (2010) to calculate initial spring force, spacer grid spring normal stiffness, spacer grid dimple tangential stiffness and dimple contact area.

Table 1: Input Parameters for Fretting Wear Calculations

Parameters	**Values**
Initial spring force, F_{BOL}	14.5N
Initial Spring Stiffness, K	34 N/mm
Rod vibration frequency of 1st mode,f_1	56 Hz
Max. RMS displacement at dimple,Y_{dn}	8.54×10^{-6} mm
Dimple tangential stiffness, K_{dt}	1306 N/mm
Co-efficient of friction, μ	0.3
Hardness, H	92 kg/mm^2
Wear Co-efficient, S	1.0×10^{-7}
Residence time, t	3 cycles

Wear Depth

It has been reported Rubiolo P. R. and Young M. (2009) that the wear marks produced on surface of fuel rodby the dimple contact are much more severe than the spacer grid spring mainly due to: i) the spring being a flexible support partially absorb the impact, whereas the dimple has a rigid contact with the fuel rod; ii) the contact area is smaller for a dimple than a spring and for an equal force, the pressure exerted by a dimple is higher than the one applied by a spring resulting in deeper wear marks; and iii) the difference in specific geometry of dimples and springs. Therefore, in the present study, the fretting wear depth '*h*' of the fuel rod has been calculated by dividing the wear volume '*V*' with the dimple contact area, 'A_d'.Mathematically;

$$h = V/A_d \qquad (6)$$

Where

h = Wear depth (mm)

V = Wear volume at EOL (mm^3)

A_d= Dimple contact area (mm^2)

The wear volume due to FIV is calculated using Equation 1, whereas, the contact area between dimple and fuel rod surface is calculated by turning on contact status tool option of ANSYS software. The contact status tool precisely predicts the sticking area of fuel rod and spacer grid dimple sat the contact points.

Results and discussion

It is believed that the maximum spring relaxation due to irradiation would take place at middle spacer grids(# 4 & 5).Therefore, fretting wear calculations for the CNPP fuel rod have been performed forth 4^{th} spacer grid. Similar observations have also been made by Kim et al (1998) while developing the fretting wear methodology for predicting the capability of a newly designed spacer grid. The results of these calculations are presented and discussed below.

Wear Volume

The parameters (given inTable 1) are used to solve simultaneously the Equations 2 and 3 for residual spring force and effective sliding distance. The value of spring relaxation is chosen such that the necessary condition of Equation 3 for the onset of fuel rod slippage must hold true. Based on the spring relaxation and other parameters the residual spring force is calculated from Equation 2. The effective sliding distance due to the rod slippage is calculated for the fuel residence time within the reactor core. The calculations are iterated between the residual spring force and the effective sliding distance in order to determine the onset of fuel rod slippage by varying the spring relaxation and cladding creep down while keeping the other parameters constant. The results for the residual spring force and effective sliding distance of fuel rod as a function of spring relaxation is shown in Figure 3.

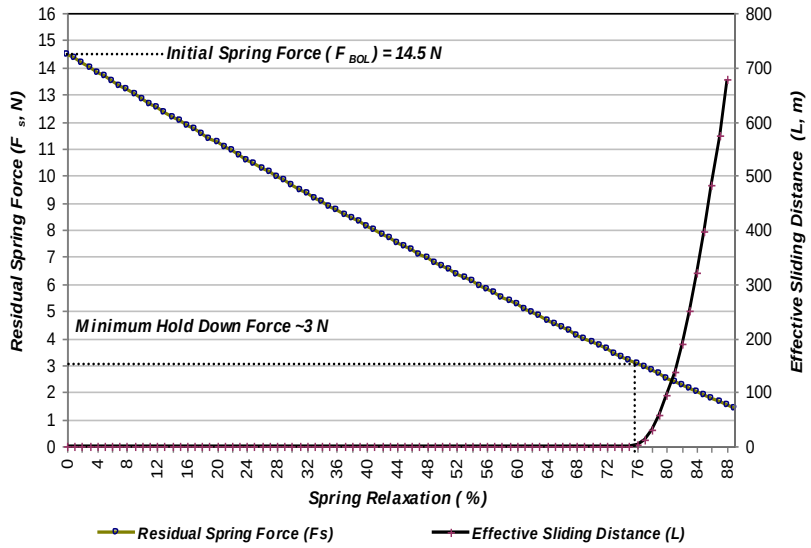

Figure 3: Residual Spring Force and Effective Sliding Distance VsSpring Relaxation

It is observed that the initial spring force decreases with the increase in spring relaxation. Whereas, the effective sliding distance remains negative until the relaxation reaches ~76% value, at which the slippage of fuel rod just starts. After the start of slippage, the residual spring force continues to decrease with the same rate, while the commutative/effective sliding distance sharply increases, with the spring relaxation. This is due to the fact that as the gap between the fuel rod and the dimple/spring progresses, the slip amplitude also increases which ultimately may lead to the perforation of fuel rod cladding due excessive fretting wear. If tube is perforated, radioactive fission products comes out of the fuel resulting in an increase in radioactivity level of the reactor coolant.

In order to prevent the cladding wear failure, the minimum hold-down force of spacer grid spring can also be calculated which is required to prevent the fuel rod fretting wear induced by FIV. Assuming that the effective sliding distance in Equation 3 as zero and doing some manipulations, the minimum hold-down force of spacer grid spring can be derived as follows:

$$Fs = (2K_{dt} \times Y_{dn})/\mu \qquad (6)$$

Where

F_s= Minimum hold-down force (N)

K_{dt}= Dimple tangential stiffness (N/m)

Y_{dn}= Maximum RMS displacement at dimple location (m)

μ= Co-efficient of friction between fuel rod and spacer grid

This Equation is similar to the formula proposed by Schrugar in 1970 F2.6, A Computer Code, FRPV, (1994) to calculate the minimum hold-down spring force. From Equation 6, the minimum hold-down spring force for CNPP fuel rod at EOL is determined to be ~3.0 N.

The calculations for the fretting wear volume of CNPP fuel rod are carried out for the third cycle year in five steps with a step of 0.2 year. From Equation 1, it appears that the wear volume of fuel rod is independent of fuel residence time but it is directly influenced by residual spring force and effective sliding distance. This does not hold true because the effective sliding distance is governed by the residual spring force and residence time. The wear volume is directly proportional to residual spring force and the effective sliding distance has an inverse relation with residual spring force. Thus the residual spring force will govern the effective sliding

distance which means that larger the residual spring force the lesser will be the slippage at dimple location (Equation 3).

The results for the fretting wear volume of the fuel rod for various creep down (0.053 –0.059 mm) and spring relaxation (76–88 %) for third cycle year have been obtained and are given in Table 2.The slippage of fuel rod will not happen unless the spacer grid spring is relaxed up to ~76%, as already shown in Figure 3. The calculated wear volume at 76% spring relaxation is 1.043×10^{-6} mm^3. When the spring relaxation is increased to 79%, the wear volume is increased almost by a factor of 8. This is due to fact that the main contribution in wear volume comes from the effective sliding distance. The cumulative wear volume of CNPP fuel rod during its residence time is determined to be 4.7332×10^{-5} mm^3.

Table 2: Fretting Wear Results

Creep-down (mm)	**Spring Relaxation (%)**	**Residence Time (Years)**	**Wear Volume (mm^3)**	**Wear Depth (µm)**
0.0526	76	0.2	1.0428×10^{-6}	0.21
0.0542	79	0.2	7.0849×10^{-6}	1.42
0.0558	82	0.2	1.1274×10^{-5}	2.25
0.0574	85	0.2	1.3656×10^{-5}	2.73
0.059	88	0.2	1.4274×10^{-5}	2.85
Total		**1.0**	**4.7332×10^{-5}**	**9.46**

Note: Calculations are performed for the third cycle year of fuel residence time in reactor core.

It may be noted that the fretting wear is basically a cyclic process. As grid to rod gap due the spring relaxation increases, the relative motion or slip amplitude between contacting surface also increases. In the present study, the effect of spring relaxation on fretting wear volume has been studied by fixing all other parameters. The wear volume is calculated by considering spring relaxation between 76–90%. The wear volume as a function of spring relaxation is shown Figure 4. This result shows that the wear volume increases with the increase in spring relaxation and is linear in nature. For 76% spring relaxation the wear volume is only about 1.043×10^{-6} mm^3. The wear volume increases with the increase in spring relaxation and reaches to a value of about 3.122×10^{-5} mm^3 when the relaxation is 90%. However, these predicted results needs experimental verification.

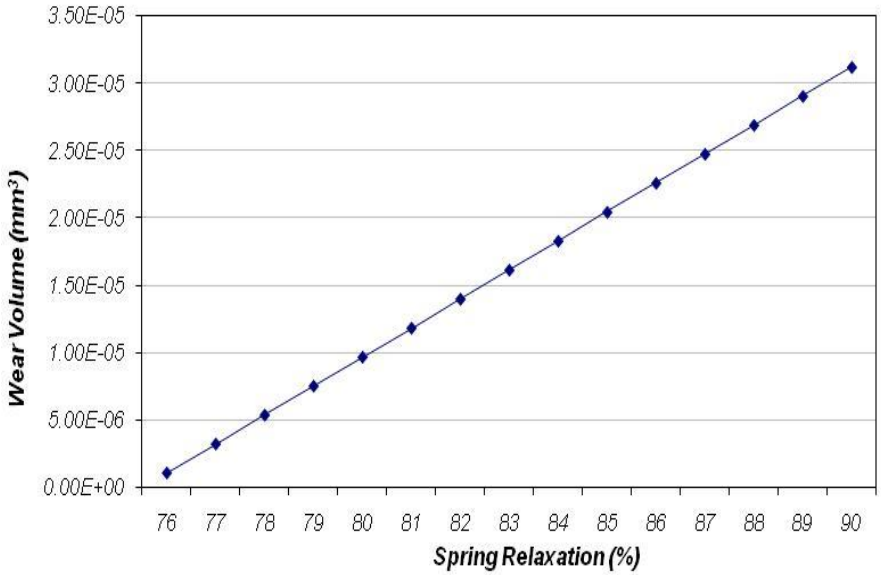

Figure4: Fuel Rod Wear Volume as a Function of Spring Relaxation

Wear Depth

The fretting wear depth of the fuel rod is determined by dividing the wear volume with the dimple contact area. The contact area between the dimple and the fuel rod surfaces is calculated to be 0.0052 mm^2usingANSYS software. It is noted that, being a rigid body, only a small contact area of dimple is formed. The calculation results (Table 2) indicate that the wear volume and wear depth increases with the residence time. The calculated fretting wear depth of the CNPP fuel rod during its residence time is 0.0095mm (9.5 μm) which is less than 10% of the wall thickness (i.e. 70 μm) of the cladding at EOL.

Conclusion

A calculation methodology has been developed to determine the fretting wear tendency of CNPP fuel rod during its residence time within the reactor core. This methodology is coupled with the FRV, FRPV, FRCB and ANSY computer codes to calculate the fretting wear volume and wear depth of fuel rod. Following conclusions are drawn from this study.

i) The residual spring force decreases with the increase in spring relaxation due to irradiation. The onset of rod slippage occurs when 76% spring relaxation is reached.

ii) The cumulative or effective sliding distance sharply increases with a slight increase in spring relaxation after the start of slippage.

iii) The fretting wear volume / depth of the fuel rod is strongly influenced by the effective sliding distance and residence time.

iv) The minimum hold-down force at EOL which is required to avoid rod slippage (the prerequisite for fretting wear), is determined to be 3.0 N.

The maximum wear depth of CNPP fuel rod due to flow induced vibration (FIV) based on the various important design parameters is calculated to be 9.5 μm which is less than 10 % of the cladding wall thickness (i.e. 70 μm) at EOL.

Although, the wear model can be applied with a good confidence not only to predict the onset of fuel rod slippage but also to calculate the fretting wear depth .However, in reactor of wear coefficient, cladding creep and spring relaxation data is necessary to validate the analytical results.

Nevertheless, the development of fretting wear model, is very useful in improving the current understanding of the fretting wear phenomena which is important not only for determining the fuel rod support condition but also to limit fretting wear damage of fuel rod within the acceptable limits for its designed lifetime.

References

[1] Chen S. S. and Wambsganss W. M., Apr (1971) Tentative Design Guide for Calculating the Vibration Response of Flexible Cylindrical Element in Axial Flow, Report No. ANL-ETD-71-07, Argonne National Lab., USA.

[2] Burgreen. D, Byrnes J. J., and Benforado D. M., (1958) Vibration of Rods Induced by Water in Parallel Flow, Trans. of ASME (American Society of Mechanical Engineers), Vol.80,.

[3] Quinn E. P. (1962) Vibration of Fuel Rods in Parallel Flow, Report No. GEAP-4059, General Electric Company, USA.

[4] Sogreah H., (1962) Study of Vibrations and Load Losses in Tubular Clusters, Initial Special Report No. 3, EURATOM - EURAEC-288, SocieteGrenobloised'Etude et d' Applications Hydrauliques, Grenoble, France,.

[5] Pavlica R. T. and Marshall R. C., (1965) Vibration of Fuel Assemblies in Parallel Flow, Trans. of ANS(American Nuclear Society), Vol.8, 599p.

[6] Paidoussis M. P., (1968) An Experimental Study of the Vibration of Flexible Cylinders Induced by Axial Flow, Trans. of ANS, 11, 352p.

[7] Morris A. E., (1964) A Review on Vortex Shedding, Periodic Wakes, and Induced Vibration Phenomena, Trans. of ASME, J. Basic Engg., 85, 185p,.

[8] Kang H. S. et al, Dec (2001) FIV Analysis for a Rod Supported by Springs at Both Ends, Journal of Korean Nuclear Society (KNS), Vol. 33, Number 6, pp 6190~6,.

[9] Perumont A, Sep (1982) On the Vibration Behavior of Pressurized Water Reactor Fuel Rods, Nuclear Technology, Vol. 58.

[10] Kim Y. H., et al, Aug, (1997) Fretting Wear of Fuel Rods due to Flow Induced Vibration, Transactions of the 14th International Conference on Structural Mechanics in Reactor Technology (SMIRT 13, paper C04/4), Lyon, France, pp 17-22.

[11] Shuffler C.A, Sep. (2004). Optimization of Hydride Fueled Pressurized Water Reactor Cores, MS Thesis, MIT, USA.

[12] Tong L. S. and Weisman J., (1996) Thermal Analysis of Pressurized Water Reactors, Third Edition by American Nuclear Society, La Grange Park, Illinois USA.

[13] Rubiolo P. R. and Young M., (2009) On the Factors Affecting the Fretting-Wear Risk of PWR Fuel Assemblies, NED, Vol. 239, pp 68-79,.

[14] Chashma Nuclear Power Plant Unit-2, Final Safety Analysis Report (FSAR), Mar (2009) Chapter 4 Section 4.2, SNERDI, China,.

[15] F2.6, A Computer Code, FRPV, Jan (1994) for the Spectral Analysis of the Fuel Rod Vibration under Parallel Flow PWR, SNERDI, China,.

[16] A18.21, A Computer Code, FRV, Jan (1994) for the Calculation of Natural Frequencies and Mode Shapes of Fuel Rod Vibration, SNERDI, China.

[17] A18.22, Oct (1993) A Manual for computer Code, FRCB, for the Calculation of the Fuel Rod Creep Bowing in PWR, SNERDI, China.

[18] ANSYS Release 13.0, (2010) CFD Software ANSYS Inc. USA,

[19] Kim K. T., Kim H. K., and Yoon K. H., (1998) Development of a methodology for In-Reactor Fuel Rod Supporting Condition Prediction", (JOKNS), Volume 28, No. 1,.

Nuclear Power Plant Surveillance Monitoring by Vibration and Acoustic Signals

Ghulam Mustafa

ABSTRACT

The purpose of this paper is to provide analytical tools for the analysis of the vibration of structure exposed to a fluid flow. Since the paper is basically emphasis on the sound and acoustical analysis of some experimental results, so it assumes some knowledge of acoustic analysis and structural vibration.

The paper highlights the causes of loose parts and the economic impacts of the detection of these detach parts. The most common consequence of loose parts is the ageing of the material. Steam generator tubes can also be broken or blocked. The Loose Parts Monitoring Technique employ vibration accelerometers for the detection of acoustic waves or bursts produced through the metal-metal impact of the loose parts with the structure surface.

The paper emphasized on the basic techniques to localized the loose parts and signals analysis. The characteristics of metal-metal impact are calculated with the help of Hertz impact theory, plate wave propagation theory, Lamb diagram of sound wave dispersion modes and sound intensity attenuation calculations.

Keywords: Vibration Analysis, Plant Surveillance, Loose Parts Monitoring, Structural Integrity and Flow Induced Vibration

Introduction:

A loose part is an object, which has been left in the system during maintenance, or an internal component dislodged during operations. Loose parts are transported by the flow of the coolant pumps, in the primary loop consisting of the reactor pressure vessel, the main coolant pumps, and the steam generator reactor cooling piping. The presence of a loose (i.e., disengaged and/or drifting) object in the primary coolant system can be indicative of degraded reactor safety resulting from failure or weakening of a safety-related Component. A loose part, whether it is from a failed or weakened component or from an item inadvertently left in the primary system during construction, refueling, or maintenance, can contribute to component damage and material wear by frequent impacting with other parts in the system. A loose part can pose a serious threat of partial flow blockage with attendant departure from nucleate boiling (DNB) which in turn could result in failure of fuel cladding. In addition, a loose part increases the potential for control rod jamming and for accumulation of increased levels of radioactive crud in the primary system.

Related Danger:

The loose parts circulate along with the coolant flow and may cause blockage in the reactor core or stream generator tubes. The flow blockage core has very serious consequences since it may load to partial fuel melt down. Stream generator tank looses would also cause expensive plant outage and repair cost. The metallic loose parts circulating in the coolant flow loops of nuclear and thermal power plants are a serious hazard for the plant safety and cost economics. These objects may cause partial coolant blockage through the boiler tubes or reactor core resulting in the failure of boiler tubes or reactor fuel. Widespread component damage has been reported internationally in power plants due to this phenomenon. In nuclear industry, the safety regulations make it mandatory to detect, identify and localize the loose parts in nuclear power plants. Due to this in every pressurized nuclear power plant in advanced country have this system.

Basic Task:

Our task is to detect loose parts, which occur in the primary coolant loop before they can cause significant damage to reactor internals. As a result of metal-metal impact a ringing sound is produced which propagates through the reactor structure. The piezoelectric accelerometer sensors are located at key location detect this sound, and with the help of detailed analysis of the sensors signals, the location of the loose parts are determined. The constraints for our detail analysis are capable of detecting metallic loose parts with high accuracy.

Literature Review:

The paper especially focuses on theoretical and analytical solutions to the problems of Loose Parts Monitoring techniques, possibly combined with other traditional computing tools. Dr. C. W. Mayo & J. M. Doster (December 1995), the purpose of this research was to establish quantitative relationships between the detected reactor loose part signal properties and the loose part damage potential. Two important open issues concerning the validity of Hertz impact theory for in-water reactor loose part impact and for the typical range of loose part impact energy were clarified experimentally. A linear correlation between plastic deformation volume and impact energy in a single impact was verified for different impact contact shapes. As the internal structures rest intermittently on the reactor vessel, the impact could originate from them, with the waveforms transmitted via the structure support.

The Loose Parts Monitoring technique employ piezo-electric vibration accelerometers for the detection of acoustic waves or bursts produced through the metal-metal impact of the loose parts with the structure surface. This paper describes the Localization of the loose parts (impact location) by rigorous analyses of sensor signals by applying various techniques of band pass filtering, acoustic modeling, and signal frequency spectrum analysis, probability distributions and cross correlation. The characteristics of metal-metal impact are calculated with the help of Hertz impact theory, plate wave propagation theory, Lamb diagram of sound wave dispersion modes and sound intensity attenuation calculations. The loose part mass is determined by comparing measured and calculated burst central frequencies and impact contact times, and the loose part impact energy is estimated by a comparison of accelerometer signal magnitude with calculated plate wave acceleration. The triangulation and the hyperbola intersection methods obtain localization of the loose part.

Loose parts localization Techniques:

The operation of a reactor is generally associated with background noise and sound events caused by the operation. These are caused by the coolant flow, by the discrete frequency sound from pumps and by the operation of other components such as valves and control elements. Additional structure-borne sound signals are generated when detached parts meet the inner walls of the reactor pressure vessel and internal fittings or when loose parts knock against internal fittings within the boundary. These individual sound events, the so-called bursts, must be unambiguously distinguished from the background noise and located. For this purpose, the intensity of the structure -borne sound signals measured is monitored in a specific frequency range. When specified limiting amplitude values are exceeded, an event alarm is emitted. In addition, it is possible to listen to the background noise and to analyze and record it that regular intervals in order to provide reference measurements so that, when the sound events cannot be unambiguously assessed, the noise pattern and the signal pattern can be compared with the reference patterns in order to from a judgment.

Delay time differences between associated sound patterns, as measured by sensors positioned at different points, are used as the criterion for distinguishing between detached and loose parts, i.e. between stationary and spatially varying impact locations. in the case of detached

parts, statistically varying values occur. Localization of loose parts using accelerometer sensor signals can be very difficult in practice. In some cases the loose part impact may be registered on one sensor alone and in such cases no conclusive results about the source location can be obtained. In other instance where bursts in several monitoring channels appear, the localization methods using time lags between bursts in different signals sometimes give erroneous results due to a large noise contamination. The main sources of error in the localization of loose parts are as follows:

The sound waves emitted from the impacting loose part have multiple frequency components. These waves having different frequencies travel with different velocities. It is therefore very difficult to accurately determine the relative delay time in different LPMS sensor signals. To resolve this problem an average sound wave velocity is used to calculate the transit-time, i.e. time required for the sound to travel from the source to the sensor. The wave velocity in the S0 and A0 modes is obtained with the help of Lamb diagram.

The sound waves traveling from the source (loose part) to the sensors undergo attenuation in intensity while traveling through the metallic structure. The attenuation in sound energy is non-linear and depends strongly upon the path geometry. It is therefore expected that the signals from different LPMS sensors would have marked difference in their time and frequency composition.

The irregular boundaries of the reactor structure, viz. pipe branching, elbows etc. cause distortions in sound wave propagation, which contribute towards the errors in loose part localization.

Plate Wave Transitions:

For bending waves which is the dominant mode for plate stress wave transmission. The propagation speed of the wave is a function of both the wave frequency and the plate thickness. Bending waves therefore exhibit dispersion, i.e. different frequencies propagate at different velocities resulting in a wave shape, which is a function of distance. The observed time required for bending wave to travel over a given distance reflects a group velocity that is a function of dominant frequencies in the detected signal. The dependence on velocity means that the wave propagation speed is different in component of different thickness. Typical wave velocities for LPMS signals of interest lie in the range 1-3 x 10^{3} ms -1.

Theory of Loose Parts Impact:

Hertz theory defines the motion of initial point of contact between a solid metal object and an infinite plate as a half sine function with half period and amplitude corresponding to the impact contact time and the peak displacement during the time of contact. The impacting object mass, velocity governs these parameters at the time of initial contact, and radius of curvature.

The equations to define peak displacement, velocity acceleration, and force for impacting object are given from equation 1-6.

$$D_{\max} = k_h (mv^2)^{0.4} R^{-0.2} \quad \text{----------1}$$

$$V_{\max} = \pi k_h / t_h (mv^2)^{0.4} R^{-0.2} \quad \text{-------2}$$

$$A_{\max} = k_h{}^{-1} m^{-0.4} v^{1.2} R^{0.2} \quad \text{----------3}$$

$$F_{\max} = k_h{}^{-1} (mv^2)^{0.6} R^{0.2} \quad \text{----------4}$$

$$t_h = \pi k_h m^{0.4} v^{-0.2} R^{-0.2} \quad \text{----------5}$$

$$k_h = ((1-\nu_1^2)/E_1 + (1-\nu_2^2)/E_2)^{0.4} \quad \text{---6}$$

m = mass of the object
v = initial velocity of the object
R = radius of curvature at point of contact
ν1, E1 = Poisson Ratio and Young's modulus for plate,
ν2, E2 = Poisson Ratio and Young's modulus for the object

Plate Wave Frequency:

The initial plate motion at point of impact is translated into a cylindrical wave that expands away from the impact location. These waves are attenuated as they travel from source to sensor. The attenuation is a complex phenomenon and depends upon bends in structural material the attenuated waves are sensed by the sensors. The initial plate motion at point of impact due to the impact force is translated into a cylindrical wave that expands away from the impact location. This wave has a different shape and frequency content than the initial half-sine motion at the point of contact. As the plate wave propagates through reactor structure it is detected as the acceleration signals by the acoustic sensors of plant LPMS. The magnitude and frequency of the acceleration signal from acoustic sensors therefore correspond to the plate wave intensity and frequency. The relation that governs the magnitude of the plate wave acceleration at the impact location is

$$A_{plate} = F_{\max} / M_{eff} \quad \text{----------7}$$

Where F-max is the peak impact force and M-eff is an effective mass of the plate volume, which is in contact with the impacting object at the time of impact. The relation gives M-eff

$$M_{eff} = \pi (c_b t_h)^2 h \rho_{steel}$$

(2)

Where, h = plate thickness,
Cb = bending wave velocity
ρSteel = density of steel

Sensor Triangulation Technique:
The loose parts localization technique incorporates the circle intersection method, which was introduced at Berkeley Nuclear Laboratories. In this method the triangulation technique of the arrival times of the burst event at various sensor locations is utilized to determine the distance between loose part and the sensors, as well as angles of incidence. Any loose part trapped in the pressure boundary of a nuclear power plant would generate acoustic waves. These waves will be received at different times by acoustic sensors located at different locations on the structure surface. The difference in the arrival times of an acoustic wave at the sensors locations defines the difference in distances of the emission source form these sensors. It can be shown that the emission source lies on a hyperbola defined by the difference in arrival time with the two sensors as foci. Two differences in arrival time from an array of three sensors define a pair of hyperbolae at whose point of intersection the emission source is located.

Method of solution:
The different in arrival time of an acoustic-emission wave at a pair of sensors defines the difference in distance of the emission source from the two sensors. It can be easily shown that the emission source lies on a hyperbola defined by the difference in arrival time with the two sensors as foci by the difference in arrival time from an array of three sensors define a pair of

hyperbola, in terms of the observed differences in arrival time, involve square roots making an analytic solution extremely difficult. The analytic solution for source location is however simplified when an alternative approach, similar to an Apollonian construction, is employed.

Consider an arbitrary three sensors array with sensors located at points S0 (0, 0), S1 (X1, Y1) and S2 (X2, Y2). An acoustic emission source at P(x, y), a distance r from S0, will give rise to path difference δ□ and δ2 defined by

δ1= PS1 – PS0 = t1 x v and

δ2 = PS2 – PS0 = t2 x v

S2 (X2, Y2)

Where v is the velocity of propagation in the material and t1 and t2 are the differences in arrival time measured for sensors S1 – S0 and S2 – S0 respectively.

The acoustic emission source at P(x, y) is located at the point of intersection of the circles about S0, S1 and S2 as centers with radii r, r + δ□ and r + δ2 respectively.

The equation of the three circles is respectively:

X2+ Y2 = r2

(X- X1)2 + (Y – Y1)2 = (r + δ□)2

(X- X2)2 +(Y – Y2)2 = (r + δ2)2

Taking the first equation from the other two in turn:

2xx1 + 2yy1 = (x12 + y12 – δ□2) – 2r δ□

2xx2 + 2yy2 = (x22 + y22 - δ22) – 2r δ2

Changing to polar coordinates these become respectively

2r(x1 cosθ + y1sinθ + δ□) = A1

And

2r(x2 cosθ + y2 sinθ + δ2) = A2

Where

A1 = x12 + y12 - δ□2

A2 = x22 + y22 - δ22

Therefore for (x1 cosθ + y1 sinθ + δ□) $\neq 0 \neq$ (x2 cosθ + y2 sinθ + δ2) the polar coordinate equations yield

$$r = \frac{A_1}{2\left(x_1 \cos\theta + y_1 \sin\theta + \delta_1\right)}$$

$$= \frac{A_2}{2\left(x_2 \cos\theta + y_2 \sin\theta + \delta_2\right)}$$

From which it follows

(A1x1 – A2x2) cosθ + (A1 y2 – A2y1) sinθ = A2 δ□ – A1 δ2.

Dividing through this equation by the term (A1x2 – A2x1)2 + (A1y2 – A2y1)21/2 yields.

$$\frac{\left(A_1 x_2 - A_2 x_1\right)\cos\theta}{\left[\left(A_1 x_2 - A_2 x_1\right)^2 + \left(A_1 y_2 - A_2 y_1\right)^2\right]^{1/2}}$$

$$+ \frac{\left(A_1 y_2 - A_2 y_1\right)\sin\theta}{\left[\left(A_1 x_2 - A_2 x_1\right)^2 + \left(A_1 y_2 - A_2 y_1\right)^2\right]^{1/2}}$$

$$= \frac{A_2\delta_{1-} A_2\delta_1}{\left[\left(A_1 x_2 - A_2 x_1\right)^2 + \left(A_1 y_2 - A_2 y_1\right)^2\right]^{1/2}}$$

Since, in this form, the coefficient of the cosθ and sinθ terms are less than unity, the equation takes the form cos (θ -ϕ) = K. Where

K= (A2 δ□ – A1 δ2)/ B
B = (A1x2 – A2x1)2 + (A1y2 – A2y1)21/2
And

$$\tan\phi = \frac{(A_1 y_2 - A_2 y_1)}{(A_1 x_2 - A_2 x)_1}$$

Since both the numerator in the term for $\tan\theta$ can be determined exactly from the known positions of the sensors (x1, y1) and (x2, y2), the measured emission arrival time difference t1 and t2 and the propagation velocity v, the angle θ is defined uniquely in the range $-\pi$ to $+\pi$. Let $\phi = \alpha + 2m\pi$, for m + 0, +, 1 +, 2.

By definition the term β is positive. Hence there are two solutions for ($\theta - \phi$) in the range $-\pi$ to $+\pi$ in the equation cos ($\theta - \phi$) = K: if the term (A2δ□– A1δ2) is positive the equation has a solution in both the 1st and 4th quadrants; and if the term (A2δ□ – A1 δ2) is negative the equation has a solution in both the 2nd and 3rd quadrants. That is if

β = cos-1 /K/ then

($\theta - \phi$) = $\beta + 2n\pi$ or $-\beta + 2n\pi$ for n = 0, +, 1 +, 2

It follows from this equation and that for ϕ that

0 = ($\alpha + \beta$) + 2mπ, for m = 0, +, 1 +, 2

That is θ has two solutions in the range $-\pi$ to $+\pi$.

A value of θ must yield r positive in the derivation for r shown earlier, in order to be a valid solution. The Cartesian coordinates of the emission source location can be then derived. In the large majority of cases, when only one value of θ is valid for a given pair (t1, t2) of time difference, the solution for the source location is unique. When two solutions of θ exist for a given (t1, t2) pair the corresponding source location is ambiguous, with locations corresponding to the two possible points of intersection of the hyperbolae defined by the time difference t1 and t2 observed by sensors S0, S1 and S2. Such ambiguous are ignored by location method involving iterative procedures.

In order to resolve the ambiguous solutions it is necessary to use a fourth sensor S3, located at the point (x3, y3) say, and compare the difference in arrival time t3, measured for sensors S3 – S0 with that calculated for the source location. This check also validates events located by three sensors.

Results and Discussion:

A large number of acoustic bursts were generated in the experimental measurements by applying the impact hammer to the surface of the tank with variable force and at variable distance from the accelerometers sensors. The coordinates of the three sensors were also varied in two-dimensional geometry over the radial and axial planes for these measurements.

The first graph displays the force signal of the impact hammer, whereas the three other graphs show the real-time behavior of the three acoustic burst signals generated as a result of the impact. The coordinates of acoustic sensors and impact point (in meters) on the cylinder for the particular measurement are given below:

Sensor #1 (S0): Reference sensor ;(0, 0)
Sensor #2 (S1) :(0, 0.4)
Sensor #3 (S2) :(1.4, 0)

Hammer (h) :(1, 0.2)

Fig. 1 is a graphical representation of these coordinates showing the impact location and the acoustic sensors.

It is evident that striking the impact hammer on the tank surface produces an impact force of the form of a sharp pulse of a total duration of 0.23 ms. The advantage of such sharp pulse signal is that it can excite wide range of acoustic frequencies along the surface of the cylinder. This fact is also evident from the frequency spectrum of the impact hammer shown in Fig. 3. This frequency spectrum is that of a typical bandwidth-limited white noise signal. The sharp peak at 6.6 KHz is the hammer resonance frequency. The real-time representation of the bursts signals detected by sensors S0-S2 shown in Fig. 2 is that of typical exponentially decaying bursts. The frequency spectra of these bursts show that the burst signals have multiple frequency components. The peak burst frequency varies between 1.1 KHz to 1.25 KHz for the three sensors signals. The frequency spectra of the bursts signals show that the sound waves detected by the three sensors have nearly identical frequency composition. It is therefore expected that the relative velocities of these sound waves for the three bursts do not vary much. This fact facilitates defining a common velocity of sound waves in the calculation algorithm.

To demonstrate the effectiveness of the algorithm for automatic detection of acoustic bursts and accurate computation of relative burst arrival times for the three sensors. The figure shows the early part of the acoustic bursts signals against the signal background. The automatic burst arrival time algorithm based on statistical analysis calculated the delay times between the hammer impact signal and acoustic sensor signals as below.

Delay between hammer and S0 signals: 0.33 ms

Delay between hammer and S1 signals: 0.3 ms

Delay between hammer and S2 signals: 0.195 ms.

It is evident from the zoomed display graphs that at the calculated burst arrival times for all sensors the sensors signals show a definite deviation from the signal background noise. It is therefore confirmed by actual measurements that the algorithm for automatic detection of burst arrival is capable of Impact Location Source location is based on the assumption that the actual acoustical paths to the sensors are the walls of the pressure-retaining boundary, and that the degree of acoustical transmission of sound in water is much less than that in the solid boundaries. Impact location is derived from the order of arrival and relative delay time of signals from three different sensors using hyperbolic intersection. The location process requires three steps of the burst over the background noise. This feature of early burst arrival detection results in high precision of location calculations of the loose parts.

Effect of delay time:

Effect of Delay Time Error on LP Location the calculations of distance and angle is quite sensitive to a change in the relative time delays between successive sensors signals. This is partly due to the fact that in the calculation algorithm the sound velocity is also calculated from the time delays.

Effect of sound wave velocity:

In order to determine the sensitivity of the calculations of loose parts location on the velocity of sound waves emitted by the acoustic burst, the calculations of distance and angle of incidence were made over a range of sound velocities between 1700 m/s to 3400 m/s. For a 100% change in sound velocity, between 1700 m/s and 3400 m/s, the variation in r4 is only 7%, whereas the distances r1 and r2 vary by a factor of 20% for the same range of sound velocities. The distance r3 is negative for all values of the velocity, and its value is very sensitive to the change in sound velocity. R3 is therefore not acceptable since it yields negative distance.

Conclusions and Recommendations:

The determination of loose part location (distance and angle) within reactor pressure boundary by analysis of acoustic signals is a complex problem and involves application of theories of sound wave transmission, attenuation and reflection through reactor structures. Due to high velocities of sound waves (~ 5 km/s), the acoustic signals need to be analyzed with

microsecond resolution. Also sound waves of different frequencies travel at different speeds, which make accurate determination of the relative delay times very difficult. The computation of distance and angle is done with the help of the Berkeley Method of 3-sensors parabolas triangulation technique. Significant improvements in LP location calculations were achieved by reducing errors in sound velocity determination, burst arrival times and angle of incidence. It has been shown that the loose parts localization algorithm is capable of automatically detecting the arrival times of acoustic bursts with high precision. This capability is very helpful in accurate localization of loose parts, and the loose parts can be localized within $\pm$ 20 cm accuracy. The angle of the loose parts impact can also be determined accurately. A general method has been developed for calculating the location, in two dimensions, of an acoustic emission source. The method yields an exact solution for any three-sensor configuration. It has been found that the most precise source location for a given timing capability is achieved for emission sources within the area bounded by the sensors.

This paper gives the details of localization of the trapped loose part by detailed analysis of the sensor signals from the plant loose parts monitoring system. It models the metal-metal impact with the help of Hertz impact theory, theory of plate waves propagation, Lamb diagram for modes of sound wave dispersion through reactor structure, and sound intensity attenuation calculations. Loose part mass is determined by comparing measured and calculated burst central frequencies and impact contact times, and the loose part impact energy is estimated by a comparison of accelerometer signal magnitude with calculated plate wave acceleration. The routines of signal statistical analysis, frequency spectrum computation, and delay-time by cross correlation analysis, circle intersection method, and narrow-band filtering has been developed. From the detail analysis of the acquired data we saw that the velocity of the sound propagated by the impact hammer depends upon the force of impact with which hammer might be struck. The delay time of the signals must be calculated very carefully because all our calculation depends upon these calculations. The very minor mistake can change our results in very beyond the exact values.

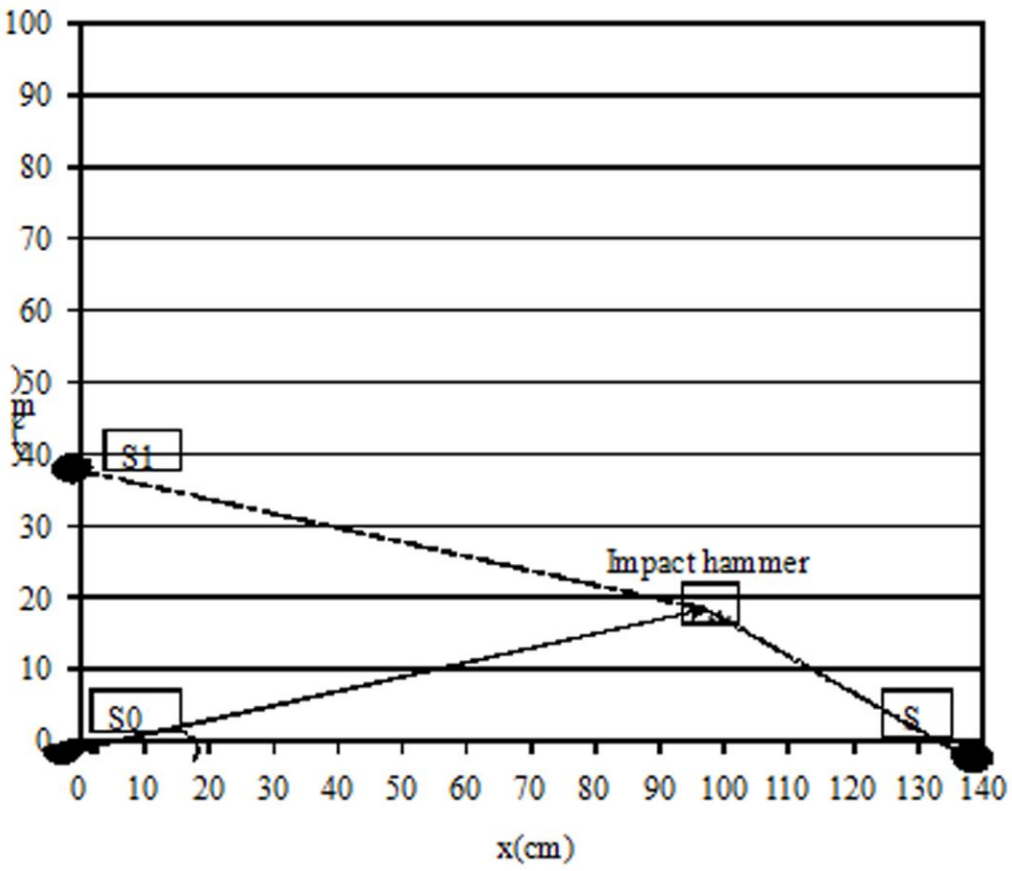

Figure 1. Graphical representation of these coordinates showing the impact location and the acoustic sensors

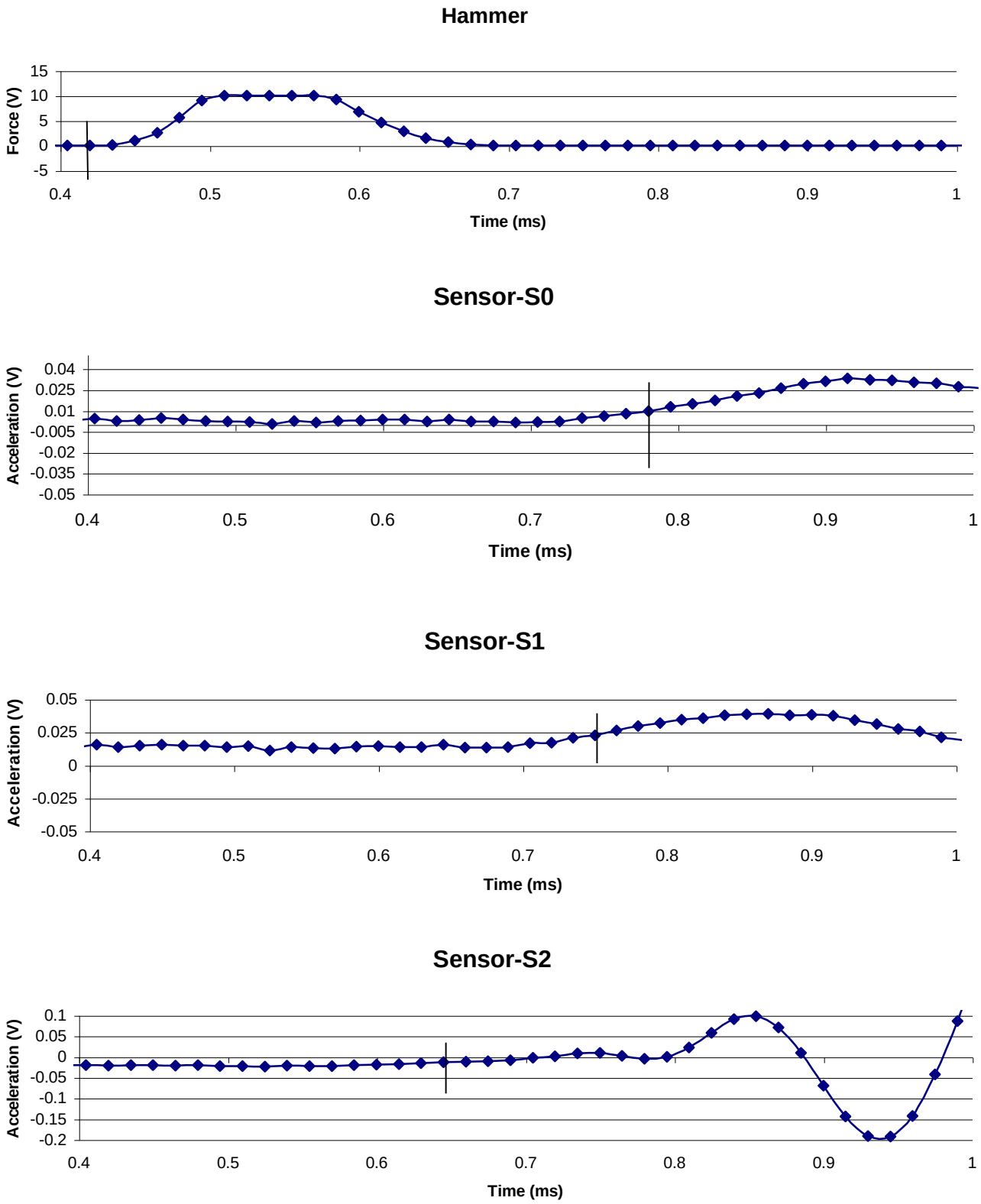

Figure 2. zoomed display of force and burst signals showing automatic detection of burst arrival

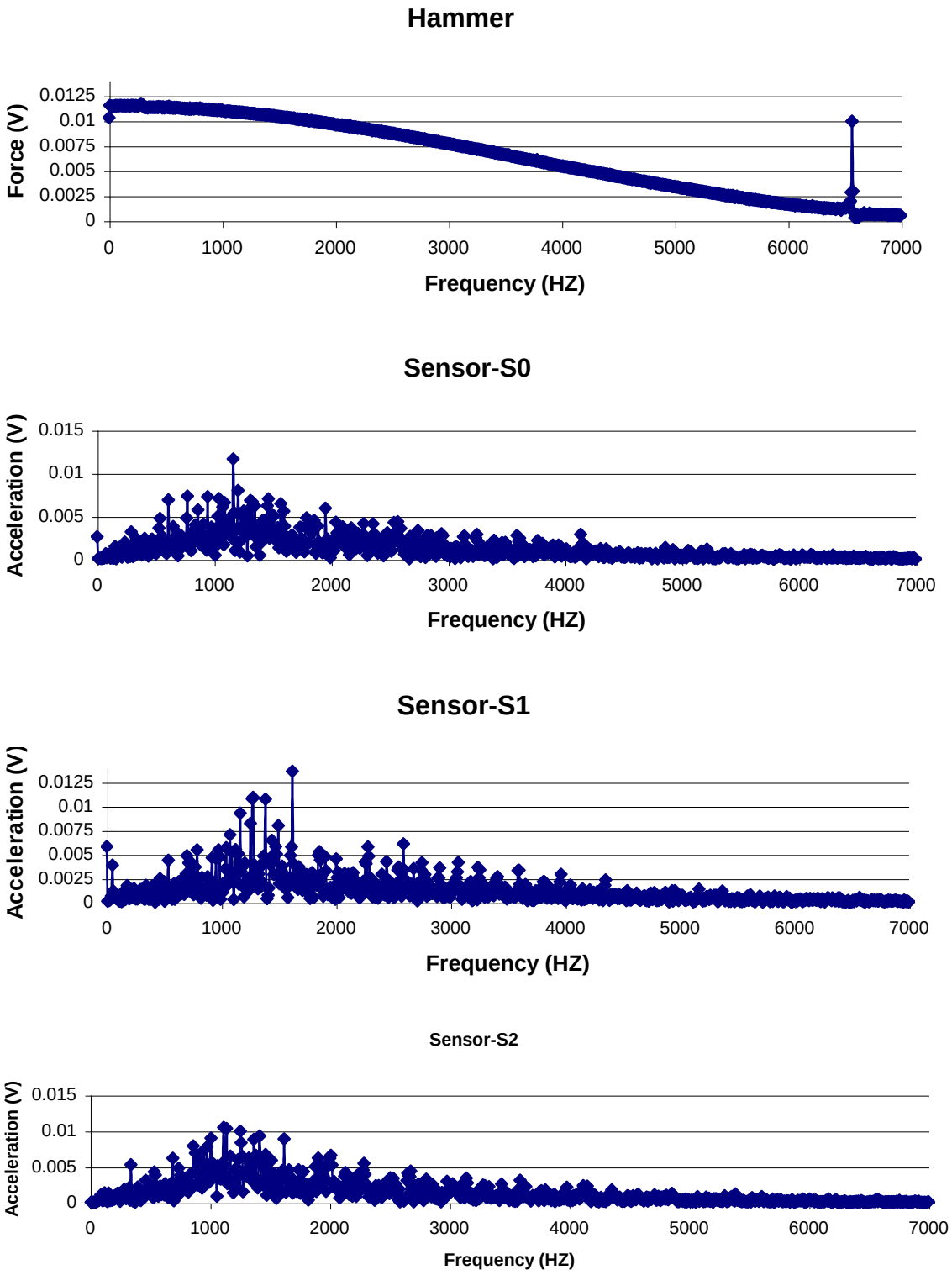

Figure3: Frequency spectra of impact force and acoustic burst signal for a typical measurement

REFERENCES

[1] Loose Part May (1981) Detection Program for the Primary System of Light Water Cooled Reactors, U.S.N.R.C. Regulatory Guide, 1.133.

[2] Acoustic Monitoring Systems for Loose Parts Detection- Characteristics, Design Criteria, and Operational Procedures, IEC-988 1990.

[3] Mayo C., "Loose Parts Monitoring System Improvements", EPRI NP-5743, The Electric Power Research Institute, CA, USA, 1988.

[4] Kryter R.C., April (1984) "Loose Parts Monitoring Programs and Recent Operational Experience in Selected US and West European Commercial Nuclear Power Stations", [1]NUREG/CR-3687, Washington D.C.

[5] Shi L., "Nuclear Reactor Loose Part Impact Activity and Damage Mechanisms", Ph.D. Thesis, North Carolina State University, USA, (1996).

[6] Mayo C., Shugars H.G., (1988) "Loose Part Monitoring System Improvements", Progress in Nuclear Energy, Vol 21.

[7] Mayo C., (1995) "Metal Impact Signal Transmission Through Reactor Structures", Proc. Specialists Meeting on Reactor Noise – SMORN-VII, Avignon, France.

[8] Gerardin J.P., (1995) "Method for Evaluating the System Instrumentation for Loose Part Detection in the Primary Cooling Circuit of French PWRs", Proc. Specialists Meeting on Reactor Noise – SMORN-VII, Avignon, France.

[9] A. Tobias, Feb (1976) " Acoustic Emission Source location in Two Dimensions by an Array of Three Sensors", Journal of Non-Destructive Testing.

Application of Vibration Analysis in Technical Process Management

Muhammad Rafiq Khan[1]

Abstract:
This paper discusses technical process management philosophy, function and scope. The technical process is shown divided into four generalized constituent parts namely, i) actuators, ii) process components, iii) instrumentation and iv) controllers. An analytical classification of the vibration analysis based condition monitoring techniques is developed that encompasses all the constituent parts of the technical processes. The role and application of the vibration analysis techniques in the overall management of technical process is in relation to the contemporary condition monitoring techniques is delineated.
Keywords: Frequency domain, Time domain, Frequency-Time domain, Fault detection and diagnosis (FDD), Accommodation of faults, analytical redundancy, hardware redundancy, I/O Data-based techniques.

Introduction:

A technical process is a part of a system and can be defined as, 'the sequentially connected interdependent and linked components which, consume single or multiple resources at each step, like employees, energy, etc, to convert input (external stimuli), like material, parts, etc into the desired form (outputs). The outputs of former step then can be inputs for the next step of a process until all linked components are complete that form the process'.
The process once designed and developed along with all necessary instrumentation &control, measures are taken to make the process robust against the malfunctioning of the constituent parts of the technical process. This increases the reliability of the processes. The comprehensive strategy to detect, diagnose and accommodate the malfunctioning of all the four constituent parts of the technical processes is referred to as, 'Technical Process Management' Herbert, August, (2009).
The constituent parts of a technical process are generalized as, i) Process components, like, pipes, tanks, pumps, supporting structures, ii) Actuators, like, motors, solenoids, cylinders, etc, iii) Instrumentation, like, sensors, transducers, signal conditioners, cables, computers, etc iv) controllers, like, feedback controllers etc. The controller is a device that operates automatically by executing some established algorithm to regulate a controlled variable(s). The controller input receives information about the status of the process variable(s) and provides an appropriate output signal to the final control element. The philosophy of technical process management is depicted in the Fig. 1. It, in fact, works in a sequence performing the fault detection, isolation, and identification and then accommodation phases of the processes' constituent parts. The fault detection is an act of knowing if something is wrong or not, the isolation determines where it is wrong. The diagnosis phase deals with extractions of information about the faults. It comprised of two activities; i) fault isolation, and ii) fault identification. The identification task is about knowing the information on the fault type and its severity while the accommodation task consists of three activities, i) removal /switching over from faulty to intact equipment, ii) fabrication of reading for the faulty controller type, alert for repair or emergency shutdown for repair.

Instrumentation FDD Schemes:

The instrumentation faults detection and diagnosis usually means the FDD of sensors as the other equipment related to instrumentation have their own simple inbuilt testing and intimation facility in case a fault occurs. However the on-line sensors' faults are difficult to detect and diagnose because of their being system embedded and due to impenetrate able system boundaries.

The sensors' on-line FDD is performed traditionally using hardware redundancy, but the approach has drawbacks regarding cost of redundant hardware and inability of this method to detect incipient faults and common mode failures etc.

1. Principle Engineer, Directorate of Nuclear Power Engineering-Plants, Pakistan Atomic Energy Commission, Ibd

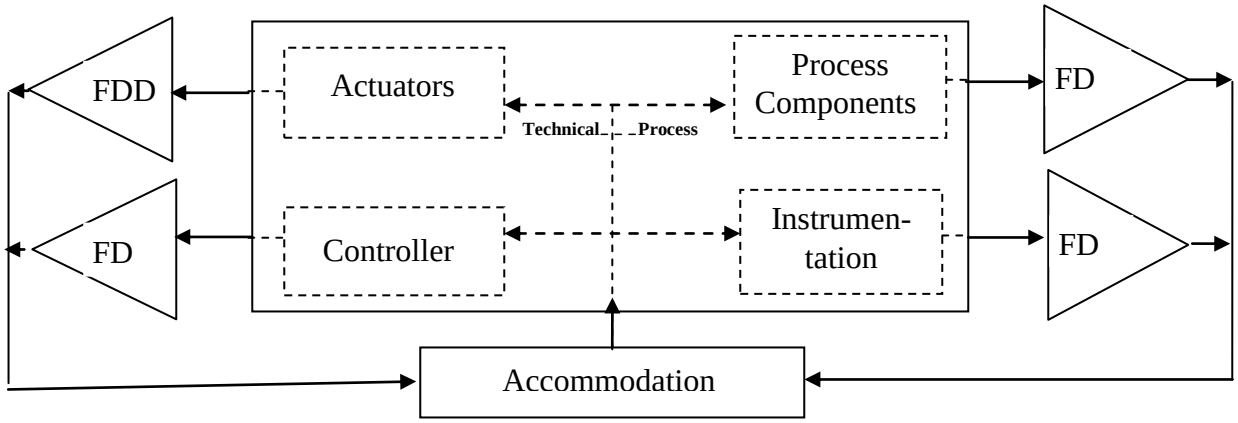

Figure 1: The Concept of Technical Process Management

equipment, etc and feeding it into the controller in case of complete failure. i.e. reconfiguration and, iii) adjustment of the faulty equipment reading in case of partial failure. The accommodation therefore takes information about a specific fault type and fault magnitude, as well as user operational criteria to determine remedial action. The accommodation tasks as mentioned above may include a change in controller gains,

Another approach is to use analytical redundancy instead of hardware to detect faults. The analytical scheme is further divided into two branches, mathematical model-based and data-driven based. The model based techniques include, parity space, observers, parameter estimation (shown in Fig. 4) techniques while the data driven methods are Principle Component Analysis (PCA) Li Shun, Fisher Discriminate Analysis Fuente, M. J., (2008) Artificial Neural Network (ANN) Azhar .S, (2010) Rahman S.A and Expert Systems techniques Paul L.F. (1986).

The Fig. 2, and 3, depicts the procedures of detection, isolation, and identification of faults of the technical process constituent parts under the process management systems. The generalized scheme of the process model-based fault detection and diagnosis is depicted in Figure 4. The aforementioned model-based techniques for sensors' FDD are equally useful for the FDD of actuators and process components, like if the coefficient of friction for an actuator begins to increase, one would suspect that a bearing has begun to fail, however several other techniques are also used for components and actuators' FDD including vibration analysis as discussed in detail in the section-4 of this paper.

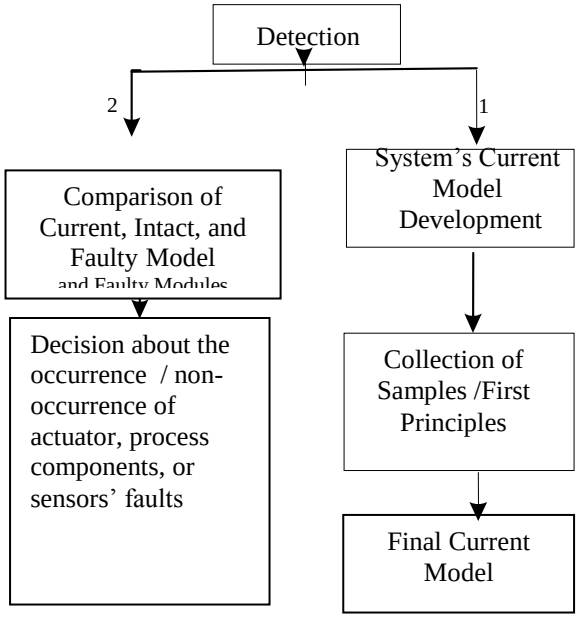

Figure. 2. Fault Detection in Technical Process Management [6]

Controllers FDD Schemes:

Controllers' faults detection and early symptoms of the likely problems is very important. The controllers / control loops may encounter various technical faults as shown in Figure 6.

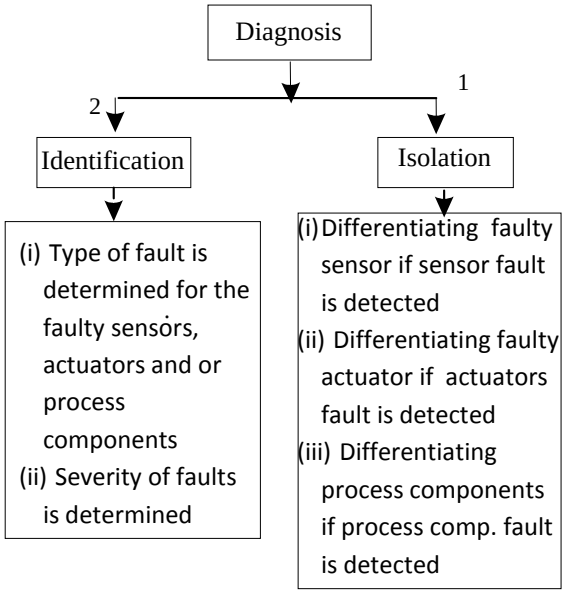

Figure 3. Fault Diagnosis in Technical Process Management [6]

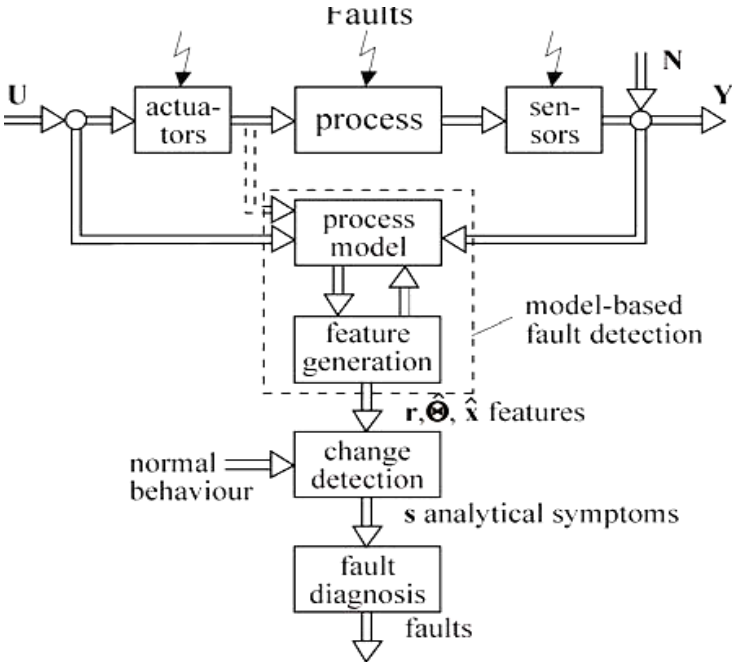

Figure 4. General Scheme of Process Model-Based Actuator, Sensor and Process component FDD [7]

The IP networks in industrial process control provide communications services for control applications and between devices as well, as shown in Figure 5. Delays or complete shutdown owing to faults in communication networks at any point in the networks may render the complete process as malfunctioning. The communication faults' FDD is done manually, however automated schemes are also being used for FDD as well as detection of early symptoms of communication problems Fault Detection in IP-Based Process Control Networks Using Data Mining, (2009).

The other types of faults are ones in which controller software and file errors are responsible for the malfunctioning of the controller. Such faults may include, a value divided by zero or reading a floating point value from EEPROM or file which has no floating point value saved inside etc. When an active controller fails, either due to software faults or hardware faults the standby controller takes over. In such situations an uninterrupted control operation is available without initialization or manual actions. The switchover generates *no* disturbances to the field output signals.

The controller faults laden processes continue to work as though nothing had happened. Redundant controllers also support the online upgrade of controller firmware. Redundant controllers can also be physically replaced online when a hardware upgrade is desired. No special cabling is required to add redundancy Emerson Process Management (2009).

The Standby controllers have the same control scheme as the Active controller. With redundancy enabled, each module calculates the required updates for the Standby controller when the module executes. The redundancy link transfers this information to the standby in milliseconds enabling controller redundancy Emerson Process Management (2009).

Application of Vibration Analysis in Technical Process Management:

As we have discussed in sections-2 and 3, the FDD of the process components, process actuators, process instrumentation and process controllers, is carried out by the model-based or data-based techniques as shown in Figs. 4 & 6. However some methods which employ signal modeling to detect and diagnose the actuator and process components faults are being used. These methods, called signal analysis methods, do not require the knowledge of the actuator or process components, or technical processes' mathematical models etc.

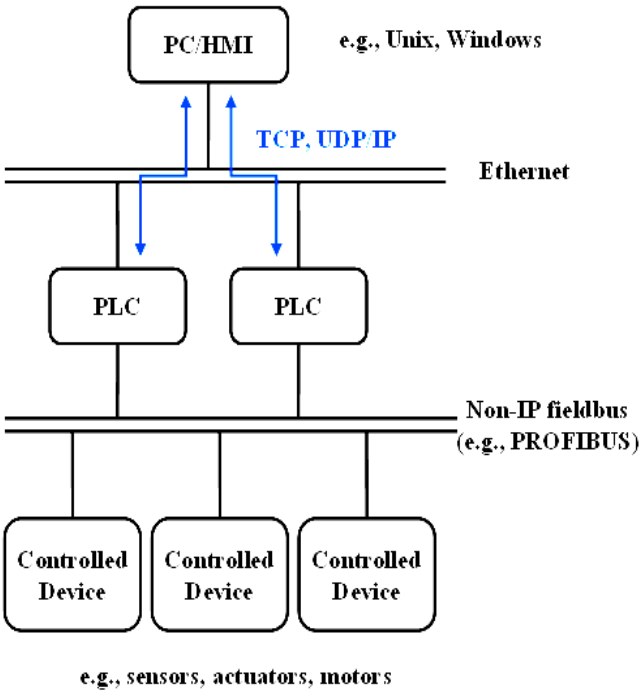

Figure 5 Architecture of Process Control Network [9]

The signal modeling methods employ analysis methods that include mechanical vibration, noise, ultrasonic, current, or voltage signals, to detect and diagnose faults. These methods are used in technical processes to monitor rotating machineries like, pumps generators, turbine engines, bearings, induction motors, gears etc.

In general by analyzing measured signals' amplitudes and frequencies and then comparing these values to the intact model of the systems the initiation and progression of machines' faults may be inferred. The signal model-based methods are relatively sensitive to the incipient faults. The vibration analysis techniques are dealt in details in the remaining sections of this paper. The ultrasonic method is applied for the bearing health monitoring as ultrasonic frequencies are produced in the early stage of bearing degradation process while the reason is lesser lubrication and wear of races. As their races begin to pit, the emissions begin to decrease in frequency. Finally, nearing catastrophic failure, the emissions intensify and move well into the audible range. The ultrasonic instrument are employed to detect vibrations in the range of

Noise /sound of the rotating machines are used to detect the malfunctioning of the rotating machines components. The method is suitable for a broad class of machining processes that emit continuous sound pattern like compressors etc. Although spectral analysis has normally been done with classic

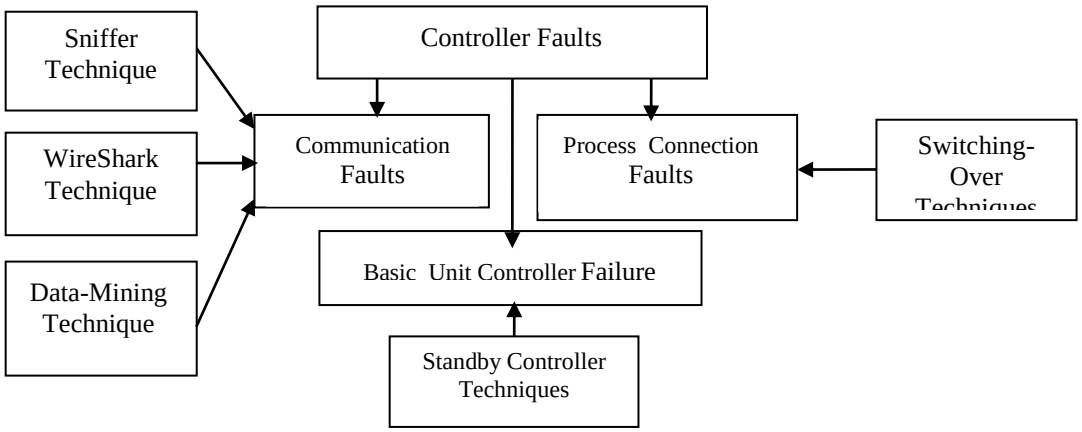

Figure 6. Controller Faults Types and Detection Techniques

20 kHz to 100 kHz. Ultrasonic signals are generated due to several types of mechanical faults. Prominent of those are rubbing or impacting types of faults.

Voltage/current spectrum is used in case of electrical motors where stator current or voltage is analyzed to find rotating machine faults. Motor current signature (MCSA) is a condition monitoring technique that is now widely used to diagnose problems such as broken rotor bars, abnormal levels of air gap eccentricity, shorted turns in low voltage stator windings, and certain mechanical problems Thomson.W.T, (2003). It is easier to detect these faults through MCSA technique as compared to vibration analysis. As shown in Figure 7, broken rotor bar produces another backward rotating magnetic field at slip speed – sNs, with side bands at 2sf1 upper and lower side.

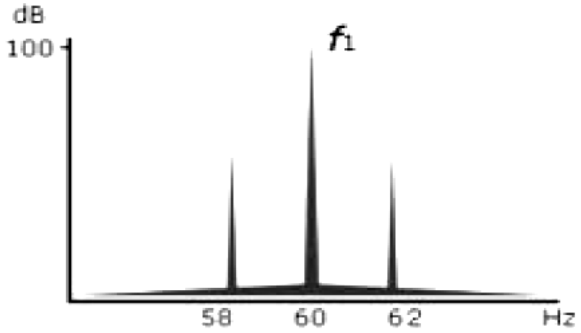

Figure 7. Idealized AC Motor Current Spectrum in Case of Two-Broken Bars

Where, f1is the supply frequency-a mathematical tools, the use of wavelet transform and beta kurtosis is currently the subject of much research.

Actuator and Process Component FDD Through Vibration Techniques:

The vibration is an oscillation wherein the vibration amplitude is a parameter that determines motion of a mechanical system etc. The types and manifestation of mechanical vibration is given in Figure 8. In vibration analysis for most of the cases it is assumed that the vibration is linear, lumped, with some degrees of freedom, may be forced or free damped or undamped etc. The mechanical vibration analysis is used for the two major constituents elements of the technical processes, i) actuator and, ii) process components. For example the electrical motors are actuators for which the vibration techniques are used for FDD while pumps and valves are the process components where vibration techniques are

extensively employed for FDD. The different vibration-based techniques for the condition monitoring can be classified as shown in Figure 9.

Model Based:

There are two types in the model-based approaches, a) AR Model Residual, b) Model Parameter Estimation.

AR Model Residual It is the vibration signal averaging technique, the proposed method first establishes an autoregressive (AR) model in the healthy-state of the rotating machine. The model is then employed to predict the future-state signal after linearly filtering error from signal. The faults of the gear, for example, are diagnosed by characterizing the error signal (residual of signals between the measured and predicted signals). The results show that the AR model technique is an effective tool in the detection and diagnosis of some machine faults like, gear faults as detection of gear cracks from vibration data is a difficult task Törnqvist .D, (2006).

a) Model Parameter Estimation

The vibration models that are developed by first principles are capable to detect incipient fault using parameter estimation in some specific machine fault like, pinion gears. In this approach wideband amplitude and phase demodulation are performed through a vibration-mode that treats all

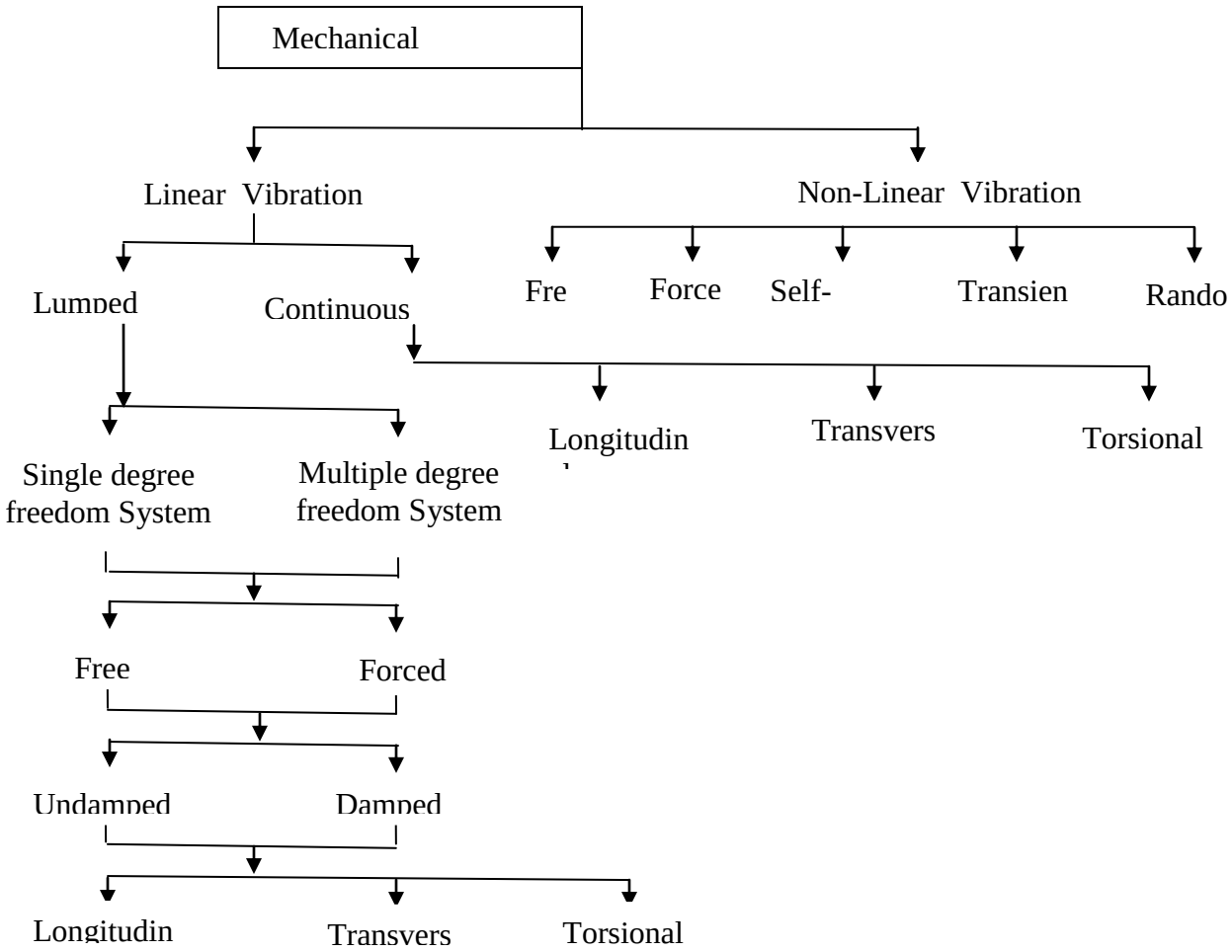

Figure 8. Spectrum of Mechanical Vibrations [11]

Disturbances and faults as part of an amplitude or phase modulation term in the model. A vibration model is given in Eq. (1), where the vibration *y*(θ) is amplitude modulated by the terma*k (θ)* and phase modulated by the term b*k(*θ*).* Where, X, is the signal amplitude, N is the sampling rate and k, is the no. of samples.

$$y(\theta) = \sum_{k=0}^{K} [1 + a_k(\theta)] X_k \cos[kN\theta + \phi_k + b_k(\theta)] \qquad (1)$$

Time Domain Analysis

Even before the use of spectrum analyzers the early condition monitoring of machines used to be in time domain. The advent of frequency spectrum analysis made the faults diagnosis apparently easier for rotating machines' faults. The time waveform analysis is getting importance again while researchers are finding it more helpful as compared to any other technique Moslemany M. EL., (1998). The time domain analysis is also relatively cheaper and used for simple less costly machines. However, this technique is not sensitive to small or early-stage defects.

a) Waveform Analysis

The vibration time waveform analysis is extensively used for the detection of gear faults. The frequency analysis is not as helpful as the time waveform in certain faults like gear faults. The time waveform provides information of the vibration amplitude against the time. There are some faulty conditions where the time-waveform performs better than the vibration analysis in frequency domain Moslemany M. EL., (1998), like, low frequency beat vibration, rotor rub, mechanical looseness, broken gear tooth, etc. In the low frequency beat the time-waveform gets modulated by low frequency beats, truncation of time-waveform and non-symmetry are indications of rotor rub, the broken gear tooth appear as impact peaks superimposed on the time-waveform with time interval equal to the inverse of 1xRPM.

b) Orbit Analysis

The orbit analysis is a technique where time vibration signals are used to plot orbits that specifically indicate certain faults. The advantage is that with this technique certain machine faults that are not readily detectable by the spectrum or mere time waveforms are detected by the orbit analysis method like, cracked shaft, loose rotating part, etc. The orbit is developed using two orthogonally located sensors. Figure 10 confirms that the shaft bow induced by the rubs causes very high synchronous vibrations during the run–up Bachschmid. N. (2004).

c) Beta Kurtosis

The Beta distribution can be utilized to rescale and shift to create distributions with a variety of shapes over a range. The beta distribution requires two shaping parameters. The kurtosis of the beta-

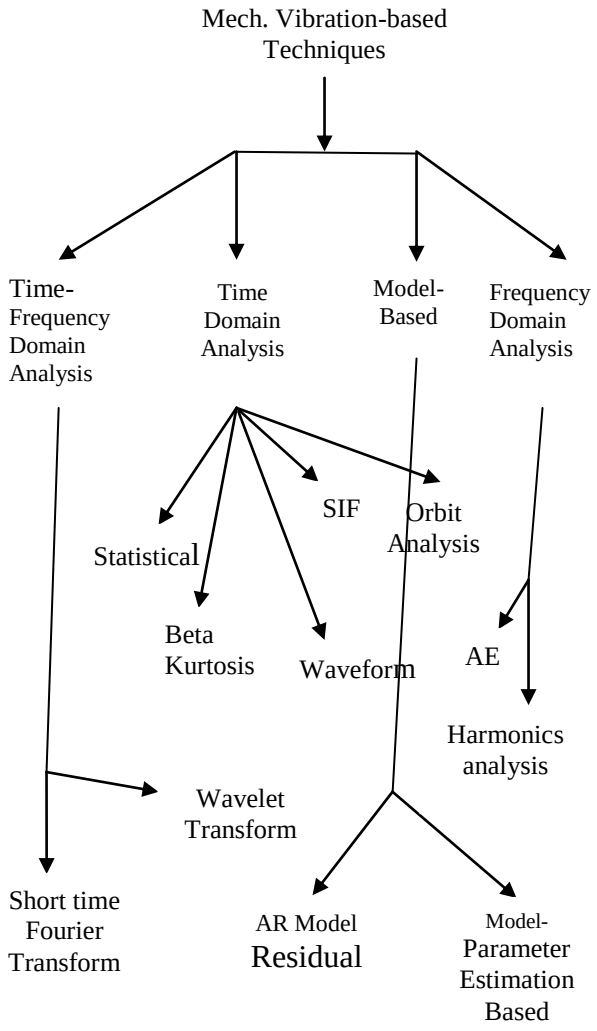

Figure 9: Spectrum of Mechanical Vibration-Based Techniques

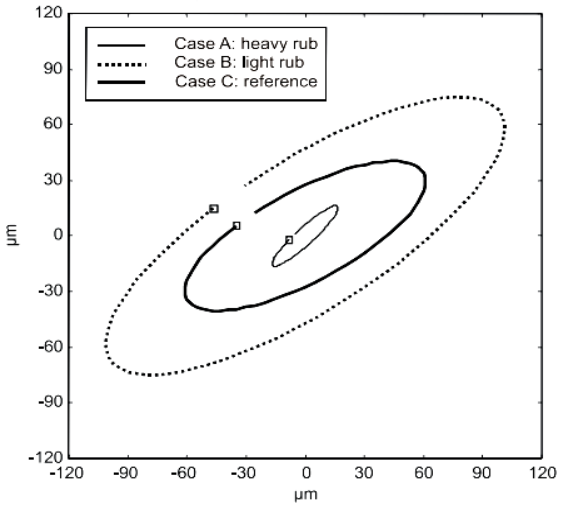

Figure 10. The Orbit Shaping in all the Three Cases Reflects Fault Occurrence [14]

Distribution has been reported in literature as a good indicator of the condition of a gear. The characteristic, or shape, parameters are usually estimated by using both the method of moments and maximum likelihood estimation (MLE) techniques. It is observed that the MLE technique provides better detection performance Wilson Q. Wang, etc. al (2001).The beta distribution describes a family of curves that are unique in that they are nonzero only on the interval (0 1). Kurtosis of the distribution is given as in Eq. 2.

$$6\frac{\alpha^3-\alpha^2(2\beta-1)+\beta^2(\beta+1)-2\alpha\beta(\beta+2)}{\alpha\beta(\alpha+\beta+2)(\alpha+\beta+3)} \quad (2)$$

$$\alpha = m\left[\frac{m(1-m)}{\sigma^2}-1\right] \quad , \beta = (1-m)\left[\frac{m(1-m)}{\sigma^2}-1\right] \quad (3)$$

m, is the mean andσ, is the standard deviation.

d) Statistical

i) RMS

The power content in a vibration signal is determined by the root mean square (RMS) value of a time vibration signal. The RMS value is the normalized second order statistical moment of time vibration signal. This is a good measure of overall noise level in the vibration signal; however RMS value does not provide any diagnosis of the faults. Detection of balance in rotating machinery is usually done by calculating the RMS values as given in Eq. (4) and (5) for continuous and discrete samples resp.

$$RMS = \sqrt{\frac{1}{T}\int_0^T (x(t)-\bar{x})^2 dt} \quad (4)$$

Where,

$$\bar{x} = \int_0^T x(t)dt \quad RMS = \sqrt{\frac{1}{N}\sum_{n=0}^{N-1}(x(n)-\bar{x})^2 dt} \quad (5)$$

$$\bar{x} = \frac{1}{N}\sum_{n=0}^{N-1} x(n)dt$$

Where, T, and N, are length of time and total number of discrete samples, respectively.

ii) Kurtosis

Kurtosis is the normalized fourth statistical moment of the signal. It indicates the relative peakiness of the signal as compared to the normal distribution. As in faults related to gear wears and breaks this feature clearly diagnoses the faults that arises due to the increased level of vibration. The equation for kurtosis in cases of discrete and continuous signals is given by, Eq. (6) & (7) for zero mean data, respectively.

$$K = \frac{\frac{1}{N}\sum_{n=0}^{N-1}(x(n)-\bar{x})^4}{(RMS)^4} \quad (6)$$

$$K = \frac{\frac{1}{N}\int_{n=0}^{N-1}(x(n)-\bar{x})^4}{(RMS)^4} \quad (7)$$

iii) Crest Factor

The RMS value measure is found to respond indifferently in the early changes of some faults like, gear and bearing damage. An alternate solution is to use another measure that is obtained by dividing the peak level of the input signal to the RMS level. The crest factor is more sensitive than RMS values if there are peaks in the time series signals. Therefore changes in the signal pattern due to impulses generated by broken tooth of a gear or an outer race defect in a bearing are readily detected. The crest factor is depicted in Eq. (8)

$$CrestFactor = \frac{Peak}{RMS} \quad (8)$$

e) SIFT

Scale invariant feature transform (SIFT)*is* a technique where features are extracted from the vibration signal through SIFT algorithm that transforms the (one dimension) vibration signal into image (two dimension).The extracted features are then classified using pattern classification techniques, instead of analyzing the vibration signal to determine the machine faults. The vibration signal can be classified to the corresponding faulty category, which presents the machine fault. Machines operating in industrial plants work in noisy environments, and as a result, the useless noise added in the recorded signals is unpreventable. As such, it may be an obstacle for analyzing the vibration signals. However, when the vibration signals are translated into images, the added noise is considered as the illumination of the light to the image Do .V.T, (2011).

Frequency Domain Analysis

a) Harmonics Analysis

The fundamental process in the frequency domain analysis is the conversion of the time domain vibration signal into frequency domain as faithfully as possible. The Discrete Fourier Transform etc is employed for this purpose as given in Eq.9, the letters and symbols in the equation carry the usual meaning.

$$X(m) = \frac{1}{N}\sum_{n=0}^{N-1} x(n)e^{-j2\pi\frac{nm}{N}} \quad (9)$$

The frequencies of the vibrations of components of a rotating machine are present in the overall vibration signature. Therefore introduction of a fault into any of these components produce change in the vibration of the corresponding frequency band of the spectrum Finley, W.R.; Hodowanec, M.M.; Holter, W.G., (1999). The harmonics and their multiples of the fundamental frequency are compared for amplitude, frequency and phase, while measuring vibration in the axial, radial or transverse direction, to match various fault symptoms.

b) Acceleration Enveloping

It is a technique that extracts the periodic impact like signal buried in the complicated time waveform New Tools for Vibration Condition Monitoring, (2011). This is useful in rolling element bearing faults detection and diagnosis. When fault occurs in the rolling element or races of the bearing the hammer like impact is felt over the structure that resonant. The signal processing is aimed at filtering out the

impact frequency from the vibration signal of high frequency. The final high pass filtered and full wave rectified signal is the acceleration envelop due to the structure resonances and bearing faults. The threshold at the amplitude of the spectral lines is used to detect the bearing faults very conveniently. The drawback of this technique is the difficulty in setting up the threshold as good baseline information is needed; especially it varies from system to system.

Time-Frequency Domain Analysis

a) Short Time Fourier Transform

The Short-Time Fourier Transform (STFT) is a powerful tool for signal processing. It specifies complex amplitude versus frequency and time for a given signal L. Satish (1998). The conventional FDD methods usually are developed and applied for constant speed machinery. For the non-stationary machinery working its operating conditions influence the vibration signal that may hide the presence of incipient faults or may mask the fault impacts due to the machine impacts. The impacts are due to the normal machine working requirement.

The STFT is therefore needed to overcome the variation of speed that remains present in the machinery speed profile corresponding to the segmented vibration signal. The time-frequency domain permits to analyze the frequency components of the vibration signal along with as time varies. The sum of STFT coefficients is compared to find the fault.

There are some drawbacks associated with STFT, firstly the window length. The wide window yields a good resolution in the frequency but poor resolution in the time domain. Second drawback is that raw STFT is computationally expensive. STFT of a continuous-time signal x (t) is defined as given in Eq. (10).

$$\mathrm{STFT}(f,\tau) = \int x(t)w(t-\tau)\exp(-j2\pi ft)dt \qquad -\infty < t < \infty \qquad (10)$$

Where, w (t) is the window function whose position is translated in time by z.

b) Wavelet Transform

Wavelet analysis is becoming a common tool for analyzing localized variations of power within a time series. By decomposing a time series into time–frequency space, one is able to determine both the dominant modes of variability and how those modes vary in time. The use of the wavelet transform is efficient for fault diagnosis, since the technique gives the information about the signal in the time and the frequency domains[20].Let x (t) denote a continuous-time finite energy signal, then WT of x (t) is defined as in Eq.(11)

$$\mathrm{WT}(a,b) = \int x(t)g_{(a,b)}(t)dt \qquad -\infty < t < \infty \qquad (11)$$

Where, $g_{(a,b)}(t) = |a|^{(-1/2)}g((t-b)/a)$ is called the base function or mother wavelet. a, b (real, a # 0) are the dilation and translation parameters, respectively. The wavelet unlike STFT performs multi-resolution analysis of the vibration signal by making use of short window for high frequencies and long window for low frequencies.

Conclusion

In this paper the overview of various functions and scope of the technical process management is given alongside contribution of mechanical vibration analysis technique is highlighted. Almost a dozen techniques pertaining to vibration analysis are mentioned. It can be gauged undoubtedly the immense potential and expected contribution of the vibration techniques in coming times, like emerging techniques of dynamic energy index (DEI) and cumulative impulse etc. are a valuable addition.

It is also observed that each technique supplements the other technique and has its own unique place and justification for its use. It is also worth mentioning that technical process management enhances process reliability, improves safety, reduces downtime, reduces maintenance cost and check events in their incipient stages that may lead to catastrophic situations.

Nomenclature /Abbreviations

I/O	Input / Output
FDD	Fault detection Diagnosis
EEPROM	Electrically Erasable
CPU	Central Processing Unit
s	slip
Ns	Synchronous speed
f	Line frequency
X	Vibration signal amplitude
y	Vibration amplitude
Θ	Discrete time
ak	Amplitude modulation term
bk	Phase modulation term
α, β	Beta kurtosis parameters
σ	Standard deviation
m	mean
g()	Mother wavelet
WT()	Wavelet Transform
STFT	Short Term Fourier Transform
SIFT	Scale Invent. Feature Transform
T	Length of time
N	No of total discrete samples
x	Continuous time signal
K	Kurtosis
a, b	Dilation & Translation paramet.

References

[1] Herbert, August, (2009) Intelligent Fault Diagnosis and Control Reconfiguration, IEEE Control Systems, (1994)

[2] Li S., A Model-Based Fault Detection and Diagnostic Methodology for Secondary HVAC Systems, Ph. D. Thesis, and Drexel University.

[3] Fuente, M. J., June (2008) Fault Diagnosis in a Plant Using Fisher Discriminant Analysis, 16th Mediterranean Conference on Control and Automation, pp. 53–58, 25-27.

[4] Azhar S., (2010) Rahman S.A., Application of Artificial Neural Network in Fault Detection Study of Batch Esterification Process, International Journal of Engineering & Technology IJET-IJENS pp. 45-51, Vol.: 10 No: 03,.

[5] PAU L., April (1986) Expert Systems, volume-3, issue 2, Wiley.

[6] Isermann .R, (2006) Fault-Diagnosis Systems, Springer.

[7] Isermann .R, (2005) Model-Based Fault Detection and Diagnosis-Status and Application, Institute of Automatic Control Darmstadt University of Technology.

[8] Fault Detection in IP-Based Process Control Networks Using Data Mining, (2009) Byungchad Park, FIP/IEEE International Symposium on Integrated Network Management,.

[9] Emerson Process Management, Sept. (2009) Delta V Product Data Sheet.

[10] Thomson.W.T., Motor Current Signature Analysis to Detect Faults in Induction Motor Drives-Fundamentals, Data-interpretation, And Industrial Case Histories, Proceeding of the Thirty Second Turbo Machinery Symposium,.

[11] Singh, (2003) Mechanical Vibration and Noise Control Handbook, Basic Concepts of Vibration, Chpater-1,Khana Publishers

[12] Törnqvist .D, Statistical Fault Detection with Applications to IMU Disturbances, (2006) M.S. Thesis, Division of Automatic Control Department of Electrical Engineering Linköpings University.
[13] EL. M. Moslemany, (1998) the Power of Time Waveform in Machinery Diagnosis, Proceedings of the 1st International Symposium on Mechanical Vibrations, Ibd.
[14] Bachschmid N., April-June, (2004) Diagnostic Significance of Orbit Shape Analysis and Its Application to Improve Machine Fault Detection, Journal of the Braz. Sco. Of Mech. Sci. &Engg.
[15] Wang W.Q., etc al, September (2001) Assessment of Gear Damage Monitoring Techniques Using Vibration Measurements, Mechanical Systems and Signal Processing., Volume 15, Issue 5., pp 905-922
[16] Do .V.T, (2011) Signal Model-Based Fault Detection and Diagnosis for Induction Motors Using Features of Vibration Signal in Two Dimension Domain, Journal of Mechanical Engineering,
[17] Finley, W.R.; Hodowanec, M.M.; Holter, W.G., (1999) An Analytical Approach to Solving Motor Vibration Problems, IEEE/ Petroleum and Chemical Industry Conference, pp.217-232,.
[18] New Tools for Vibration Condition Monitoring, Oct-Dec.2011 Hydrocarbon Asia.
[19] Satish L., Short-time Fourier and Wavelet March (1998) Transform for Fault Detection in Power Transformers during Impulse Test, IEE Proc. Sci.Meas.Technol., vol-145, N0.2.
[20] Ghafari S.H., (2007) A Fault Diagnosis System for Rotary Machinery Supported by Rolling Element Bearings, Ph. D. thesis, University of Waterloo, Ontario Canada,.